



저작자표시-비영리-변경금지 2.0 대한민국

이용자는 아래의 조건을 따르는 경우에 한하여 자유롭게

- 이 저작물을 복제, 배포, 전송, 전시, 공연 및 방송할 수 있습니다.

다음과 같은 조건을 따라야 합니다:



저작자표시. 귀하는 원저작자를 표시하여야 합니다.



비영리. 귀하는 이 저작물을 영리 목적으로 이용할 수 없습니다.



변경금지. 귀하는 이 저작물을 개작, 변형 또는 가공할 수 없습니다.

- 귀하는, 이 저작물의 재이용이나 배포의 경우, 이 저작물에 적용된 이용허락조건을 명확하게 나타내어야 합니다.
- 저작권자로부터 별도의 허가를 받으면 이러한 조건들은 적용되지 않습니다.

저작권법에 따른 이용자의 권리는 위의 내용에 의하여 영향을 받지 않습니다.

이것은 [이용허락규약\(Legal Code\)](#)을 이해하기 쉽게 요약한 것입니다.

[Disclaimer](#)

이학박사학위논문

**Two-dimensional photonic crystal  
band-edge laser using colloidal  
quantum dots as gain material**

콜로이드 양자점을 이득 물질로 이용한 이차원  
광자결정 띠가장자리 레이저

2016년 2월

서울대학교 대학원

물리천문학부

장 호 준



# **Two-dimensional photonic crystal band-edge laser using colloidal quantum dots as gain material**

by  
Hojun Chang

*Supervised by*  
Professor Heonsu Jeon

*A Dissertation Submitted to the Faculty of  
Seoul National University  
in Partial Fulfillment of the Requirements  
for the Degree of  
Doctor of Philosophy*

February 2016

Department of Physics and Astronomy  
Graduate School  
Seoul National University



# Abstract

## **Two-dimensional photonic crystal band-edge laser using colloidal quantum dots as gain material**

Hojun Chang

Majoring in Physics

Department of Physics and Astronomy

The Graduate School

Seoul National University

Semiconductor-based lasers typically utilize multiple quantum wells (MQWs) for gain materials. Despite well-known advantages of MQW structure, emission wavelength is fixed in a narrow bandwidth, and device architecture become heavily dependent on substrate. This study focuses on solving such an issue by realizing highly tunable and less substrate-dependent laser device by combination of colloidal quantum dots and photonic crystal structure.

Core-shell type colloidal quantum dots (CQDs) exhibit efficient photoluminescence with widely tunable bandgaps based on quantum confinement effect. Not only could such core-shell type CQDs be used to replace epitaxially grown semiconductor gain materials, but also be functionalized for brand-new concepts of optical devices and applications.

CQDs form a deposited film simply by conventional spin-coating method.

On the other hand, photonic crystal is a structure with periodic distribution of refractive index, in which periodicity dictates photonic band structure and photonic band gap. The useful feature has been used to fabricate lasers, waveguides and various other types of optical devices. In this study, properties of photonic band-edge mode are the focus of research, which slows the light in matter increasing the interaction in between.

This dissertation demonstrates lasing emission from a two-dimensional (2D) photonic crystal (PC) backbone with densely packed CQDs embedded within the PC as a gain material. The PC slab consists of a silicon nitride film on silica substrate, forming an asymmetric slab waveguide. Numerical analyses based on finite-difference time-domain method show that photonic band structure of a simple square lattice could have an M-point band-edge mode in the air-band. An array of air-holes is fabricated into a  $\text{Si}_3\text{N}_4$  film by e-beam lithography and reactive ion etching with various air-hole diameters. On top of the PC backbone, CQDs are spin-coated and cured, resulting in the air-holes of the PC backbone infiltrated by CQDs to provide optical gain for lasing action. Completed CQD-PC laser device is then optically pumped using a sub-nanosecond 532 nm pulsed laser. The CQD-PC laser showed double band-edge mode laser operation with emission linewidth less than 1 nm at full-width-half-maximum.

**Keyword:** Colloidal Quantum Dot, Photonic crystal laser, Photonic band-edge modes

**Student number:** 2008-20451



# Contents

## Chapter 1

<b>Introduction</b> .....	1
1.1 Limits of current status of semiconductor lasers .....	1
1.2 Alternative approach -colloidal quantum dot as a gain material .....	6
1.2.1 Colloidal quantum dots (CQDs).....	6
1.2.2 Lasers based on colloidal quantum dots.....	6
1.2.3 Selection and supply of CQDs.....	8
1.2.4 Photonic crystals .....	11
1.2.5 Selection of types of PC lattices .....	14
1.3 Summary and outline of manuscripts .....	16
References .....	17

## Chapter 2

### Device Design and Numerical Analyses for CQD-PC Band-edge

<b>Laser</b> .....	25
2.1 Introduction .....	25
2.1.1 Plane-wave expansion method.....	26
2.1.1 Finite-difference time-domain Method .....	27
2.2 Optical properties of materials for design .....	28
2.2.1 Indices of refraction: CQD film and $\text{Si}_3\text{N}_4$ slab .....	28
2.2.2 Optical properties of CQD film.....	31
2.2.3 Thickness of $\text{Si}_3\text{N}_4$ backbone slab waveguide .....	31
2.3 Design of CQD-PC laser .....	33
2.3.1 Principles of CQD-PC laser design .....	33
2.3.2 Photonic band structure of 2D square lattice PC by 2D PWE	

method-----	33
2.3.3 Photonic band structure of 2D square lattice PC by 3D FDTD	
method-----	36
2.4 Summary -----	40
References -----	41

### **Chapter 3**

<b>Fabrication of CQD-PC Band-edge Lasers</b> -----	42
3.1 Introduction -----	42
3.2 Fabrication processes -----	44
3.2.1 PC backbone fabrication-----	44
3.2.2 CQD spin-coating-----	48
3.3 Devices fabricated by laser holographic lithography -----	52
3.4 Summary -----	56
References -----	57

### **Chapter 4**

<b>Measurements, Results, and Discussion</b> -----	58
4.1 Introduction -----	58
4.2 Measurements and results-----	60
4.2.1 Micro-photoluminescence setup-----	60
4.2.2 Measurement of CQD-PC laser with nominal 80 nm-thick CQD over-layer -----	62
4.2.3 CQD over-layer analyses: T-130 device -----	65
4.2.4 Measurement of CQD-PC laser with nominal 60 nm-thick CQD over-layer -----	69

4.2.5 CQD over-layer analyses: T-80 device	73
4.3 Discussion: T-80 vs. T-130	76
<b>Chapter 5</b>	
<b>Conclusion</b>	80
<b>Appendices</b>	81
A Preparation of CQD film	81
B Modal gain and confinement factor	83
Abstract in Korean	86



# List of Tables

Table 1-2-1 one-to-one correspondence between PCs and electronic crystals 13

Table 3-1-1 Comparison between three common lithography methods -----43

# List of Figures

Figure 1-1-1 Typical architecture of semiconductor lasers----- 2

Figure 1-2-1 Colloidal quantum dots with different diameters, exhibiting various colors. ----- 9

Figure 1-2-2 Various types of lasers built with CQDs with different structures: random cavity, 1D surface grating, and vertical cavity -----10

Figure 1-2-3 representations of 1D, 2D, and 3D PCs -----12

Figure 1-2-4 SEM images of examples of PCs with sub-micron periods -----12

Figure 1-2-5 Dispersion relation between (a) momentum and energy of one electron in an electronic crystal, (b) frequency of electromagnetic fields and wave vector  $\mathbf{k}$  in a photonic crystal structure -----13

Figure 1-2-6 Schematic of CQD-PC band-edge laser structure. The  $\text{Si}_3\text{N}_4$  waveguide slab perforated with a square lattice array of air-holes serves a passive PC backbone on  $\text{SiO}_2$ -cladding/Si-substrate. Spin-coated CQDs not only infiltrate the air-holes but also form a thin over-layer. Shown together are (left) a schematic structure as well as a transmission electron microscope image of the CdSe/CdS/ZnS core-shell-shell CQD and (right) the reciprocal lattice of square lattice PC with high symmetry

points marked-----	16
Figure 2-2-1 Measured index of refraction of CQD film. The real part of refractive index is $n = 1.75$ . The thickness of measured layer is $\sim 70$ nm -	29
Figure 2-2-2 Index of refraction of $\text{Si}_3\text{N}_4$ -----	29
Figure 2-2-3 Measured photoluminescence and calculated absorption coefficient spectra of CQD film -----	30
Figure 2-2-4 Index of refraction of CQD film. The real part of refractive index is $n = 1.75$ . The thickness of measured layer is $\sim 70$ nm.-----	32
Figure 2-3-1 Typical photonic band structure of 2D square lattice PC. calculated by the PWE method. $\Gamma$ - and M- point shows stable band-edge modes -----	35
Figure 2-3-2 Photonic bands near the M-point of 2D PC. Insets show transverse electric field profiles in a unit cell of each band -----	35
Figure 2-3-3 Photonic band structure and M-point band-edge mode properties of the 2D square lattice CQD-PC structure. (a)(b) Photonic band structure calculated by 3D FDTD: (a) overall and (b) near the M-point band-edges. (c) Resonant mode spectrum calculated for the M-point band-edges, exhibiting two HIBE modes ( $M_1$ and $M_2$ ) at $\lambda \sim 622$ nm and two degenerate LIBE modes ( $M_3$ and $M_4$ ) at $\lambda \sim 610$ nm. The insets display the band-edge mode profiles (transverse E-field intensity) for $M_2$ and $M_3/M_4$ , also calculated by 3D FDTD -----	38
Figure 2-3-4 Transverse electric field intensity profiles of M-point modes properties of the 2D square lattice CQD-PC structure. (a) an HIBE mode: $M_2$ (b) two degenerate LIBE modes: $M_3$ and $M_4$ -----	39

Figure 3-1-1 Fabrication processes of CQD-PC band-edge lasers -----43

Figure 3-2-1 2D PC pattern cluster on a Si<sub>3</sub>N<sub>4</sub>/ SiO<sub>2</sub>/ Si substrate rotated 45° to maintain stable electric field distribution of the M-point PBE modes. The schematic representation of device (above) shows unit cell of 2D PC and part of mesh grid line. The 3D representation (below) depicts an ideal device emitting light to k<sub>||</sub> = (1, 1) direction with no CQD over-layer on top.-----45

Figure 3-2-2 Images of fabricated CQD-PC laser devices. (a)(b) Optical microscope images of fabricated Si<sub>3</sub>N<sub>4</sub> PC backbone with the mesh grid pattern for device identification. (c)(d) SEM images of the fabricated Si<sub>3</sub>N<sub>4</sub> PC backbone-----47

Figure 3-2-3 An SEM image of prototype testing sample. CQD spin-coating left CQD over-layer with void area (nominal thickness ~ 30 nm) above PC cluster. -----50

Figure 3-2-4 An SEM image of thick CQD over-layer above PC cluster -----50

Figure 3-2-5 SEM images of CQD-PC device after CQD spin-coating for ~ 80 nm nominal thickness (a) CQD over-layer scratched intentionally (b)confirmed CQD filling into the air-holes -----51

Figure 3-3-1(a) A schematic diagram of laser holographic lithography setup using 266 nm DPSS laser as a light source. (b) Interference pattern consisting of a periodic series of fringes representing intensity maxima and minima -----54

Figure 3-3-2 An SEM image of Si<sub>3</sub>N<sub>4</sub> PC backbone fabricated by LHL. Uniformity of air-holes was not up to the level of fabrication quality required to operate as a laser-mode supporting device backbone

structure-----	55
Figure 4-2-1 micro-photoluminescence ( $\mu$ -PL) measurement setup a 532 nm, frequency-doubled, 400 pico-second pulsed Nd:YAG laser with 1 kHz repetition rate to characterize laser emission from CQD-PC band-edge lasers -----	61
Figure 4-2-2 Micro-photoluminescence spectra measured from the CQD-PC band-edge laser devices at various pump power density levels. Nominal CQD over-layer thickness $\sim$ 80nm-----	62
Figure 4-2-3 $L$ - $L$ curve recorded from the CQD-PC laser devices with nominal CQD over-layer thickness $\sim$ 80nm -----	63
Figure 4-2-4 Polarization properties of CQD-PC band-edge lasers. (a) measurement setup with polarization analyzer in front of spectrometer (b) polar plots of lasing CQD-PC emission showing horizontal dipole polarization -----	64
Figure 4-2-5 CQD over-layer analyses with various methods. (a) AFM image of CQD over-layer on a PC cluster (b) AFM cross-sectional depth data along the red line in (a) (c) SEM image of a device top-view of nominal CQD over-layer thickness $\sim$ 80nm (d) SEM image of cross-sectional layers showing 130 nm CQD over-layer thickness -----	67
Figure 4-2-6 Mode transition of CQD-PC band-edge laser devices with various over-layer thicknesses -----	68
Figure 4-2-7 An ‘ideal device’ realized by CQD spin-coating process for an over-layer thickness thinner than T-130. For an ‘in-reality’ sample fabrication, nominal CQD thickness was set to be $\sim$ 60 nm -----	69

Figure 4-2-8 Typical micro-photoluminescence spectra measured from the CQD-PC devices at various pump power density levels. Nominal CQD over-layer thickness  $\sim 60\text{nm}$  -----71

Figure 4-2-9  $L-L$  curve recorded from the CQD-PC laser devices with nominal CQD over-layer thickness  $\sim 60\text{nm}$  -----72

Figure 4-2-10 SEM image of cross-sectional layers showing 80 nm CQD over-layer thickness: T-80 -----74

Figure 4-2-11 SEM images of CQD spin-coated devices fabricated by LHL method. (a) a top-view SEM image on 2D PC backbone (b)(c) SEM images of cross-sectional layers showing  $\sim 60$  nm CQD over-layer when spin-coated with recipes targeting nominal thickness  $\sim 60$  nm just as T-80 -----75

Figure 4-3-1 Lasing properties of CQD-PC band-edge lasers. (a)(b) Cross-sectional SEM images of two CQD-PC devices with different CQD layer thicknesses: (a) T-80 and (b) T-130, from which the CQD over-layer thicknesses were measured to be  $\sim 80$  nm and  $\sim 130$  nm, respectively. The SEM images were taken from planar part of samples for thickness characterization. (c)(d) Photoluminescence spectra measured from the CQD-PC band-edge laser devices at various pump power density levels: (c) T-80 and (d) T-130. The insets are light-in versus light-out ( $L-L$ ) curves drawn from the measured spectra:  $L-L$  curves for the HIBE (red, solid triangles) and LIBE (blue, solid squares) modes as well as spontaneous emission (brown, open circles) -----77

Figure 4-3-2 Quality factors for M-point band-edge modes of a “cold” cavity-----79



# Chapter 1

## Introduction

### 1.1 Limits of current status of semiconductor lasers

Trend of device platforms and solutions for high-density photonic integrated-circuits dictates the necessity of on-chip, integrated small-scale semiconductor lasers. As an integral part of future hybrid on-chip devices, semiconductor light sources are required to be small using less energy input and more tunable while being compatible to other parts of total architecture of devices. Semiconductor lasers have issues to address so as to meet such performance standards: issues of substrate for materials growth and narrow tunability problem as a consequence.

Due to different lattice constants of III-V semiconductor materials—widely used semiconductors with light-emitting properties due to direct band gap, each material has substrate preferences. For instance, GaN-based epi-layers for light-emitting devices are grown on a sapphire, or a SiC substrate. Figure 1-1-1 shows a typical architecture of a semiconductor laser device, which are realized on a sapphire substrate.<sup>1</sup> Growth on other substrate might lead to poor quality of epi-layers, deteriorating light-emitting qualities. Although recently GaN growth on Si substrate was reported,<sup>2</sup> overcoming huge lattice mismatch, this is highly exceptional cases that requires tremendous amount of time and efforts. Since appropriate substrates for different materials must be selected to guarantee quality of grown materials, dense integration of each different device based on a variety of substrate is hard to achieve.

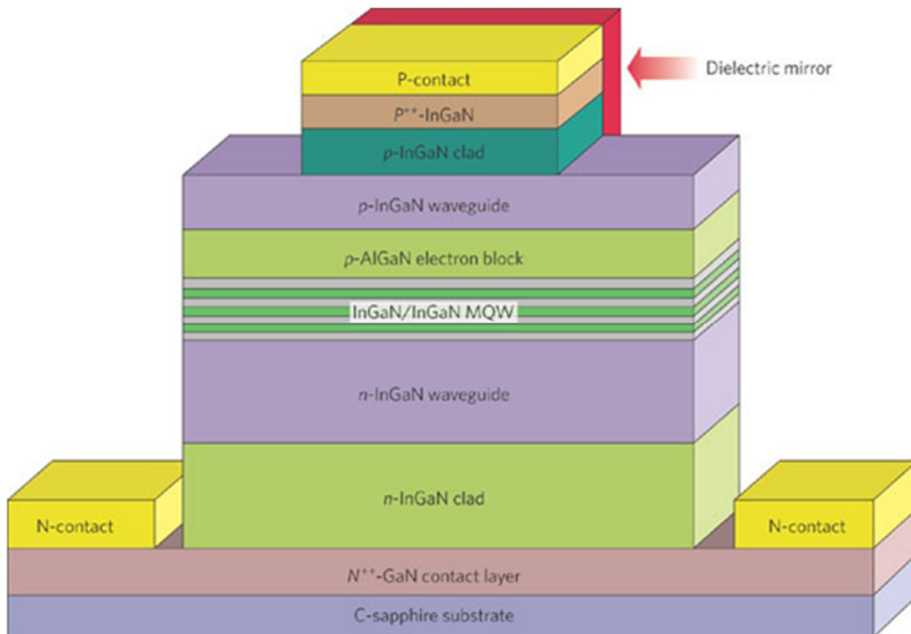


Figure 1-1-1 Typical architecture of semiconductor lasers.<sup>1</sup>

Tunability of light-emitting devices is also facing limitations. Since double heterostructure based on such semiconductor materials—commonly well-represented by multiple quantum wells (MQWs)—became a conventional form of active layer for optical gain, growth process limits tunability of materials. Wide band-gap semiconductors show broad range of emission wavelengths; however, it is limited during the growth process of active layers on a designated substrate. For example, InGaN is known to be highly tunable, wide band-gap semiconductor material whose light-emitting wavelength can vary according to indium content, and yet the indium content is fixed during conventional metal-organic chemical vapor deposition (MOCVD) process, not to mention indium content of InGaN deposition is severely limited typically under 30% due to crack of deposited layers from lattice mismatch.<sup>3</sup> This is also true for InGaAsP-based devices because band-gap

engineering of materials on a certain growth substrate such as GaAs or InP is restricted by wavelength-selective growth process. Hence, InGaAsP-based light-emitting devices are usually for infrared approximately from 1300 nm ~ 1600 nm, GaN-based light-emitting devices are practically for range from 400 nm to 600 nm depending on indium content and crystal axis of substrate.<sup>4</sup>

Despite all the limitations, advances in other fronts of research towards semiconductor nanolasers have never been ceased. In area of research on reducing modal volume and realizing semiconductor nanolasers, there has been significant progress. Although it is relatively new area of research, recent development of plasmonic lasers look prominent because they have intrinsically very small modal volume.<sup>5,6</sup> Typically, plasmonic lasers have mode area in the order of a few hundred square nanometers due to the evanescent nature of mode confinement.

However, most of plasmonic lasers suffer from high threshold, usually up to the order of  $\text{GW}/\text{cm}^2$  due to significant optical loss from metal, which is essential to plasmonic resonance, either mechanism of such devices is based on surface plasmon polariton resonance (SPPR) or localized surface plasmon resonance (LSPR).<sup>7,8</sup> Some of those devices showing the order of  $\text{MW}/\text{cm}^2$  threshold were only demonstrated in low-temperature environment less than 10K. Considering semiconductor nanolasers researches are supposed to aim less energy input, these drawbacks outshine advantages of very small mode area, naturally limiting their use for practical applications.

Photonic crystal (PC) lasers, on the other hand, have shown reasonably low thresholds, even continuous-wave (CW) PC-based laser structures were successfully demonstrated in room-temperature environment.<sup>9,10</sup> The first demonstration of PC laser by optical excitation was based on the principles of PC cavity structure in

InGaAsP material.<sup>11</sup> The device used defect modes that located at the center of 2D PC slab. The first PC laser by electrical injection is also demonstrated in the same InGaAsP materials with center defect and pillar design at the center for electroluminescence.<sup>12</sup>

However, PCs have another problem owing to its structural nature. PC lasers also conventionally use multiple-quantum-wells (MQWs) as gain material that should be perforated with air-holes to form complete PC slab, including MQW active layers. This “gain material carving out to form resonance structure” fabrication approach is inherently huge loss of expensive materials, not to mention it still has limitation from material growth just like other MQW-based semiconductor lasers.

Membrane-type architecture of PC lasers is another problem to solve. In order to fully facilitate PC-based optical resonance in a symmetric slab waveguide with sufficient contrast of refractive indices, it is required to form a membrane-type, air-bridge PC structure floating in air.<sup>13-28</sup> Usually, growth of etch-sacrificial layer and wet-etch processes are introduced, which makes overall structure mechanically fragile and hard to realize densely-packed integrated devices. In order to accomplish high-density integrated on-chip applications using PC lasers, device architecture based on this ‘unstable’ structure should be abolished.

Nano-stepping stone laser is a good example of using such an asymmetric slab waveguide for PC-based application.<sup>29</sup> This device was fabricated on fused quartz— basically a SiO<sub>2</sub> cladding layer to secure required refractive index contrast, which used InAsP MQWs for optical gain. Surely, refractive index contrast of III-V material-to-SiO<sub>2</sub> is less optimal than that of III-V material-to-air, but enough to provide optical confinement required for lasing operation of the device.

The most advanced PC laser with extremely small volume is semiconductor single quantum dot grown by molecular beam epitaxy (MBE) method. Mode volume as small as  $\sim 0.5(\lambda/n)^3$  were reported.<sup>30</sup> Semiconductor single quantum dots, are MBE-grown and placed in a PC nanocavity with high quality factor, successfully modifying spontaneous emission rate.<sup>31</sup> However, the MBE growth is not suitable for cost-effective fabrication due to use of ultra-high vacuum chamber and highly controlled, slow deposition process.

For development of novel and yet practical and functional laser device, PC-based approach still looks valid. Asymmetric slab approach can be an important take-away that can be used in the study. However, MQW-based optical gain for a new device should be replaced by much more tunable material with facile fabrication method. It was a main focus of this study to apply an efficient tunable material that can be used for a PC-based optical cavity, or a PC backbone—where optical modes for lasing is still supported by principles of photonic crystal structure, and yet optical gain material or a layer is not a part of such a passive PC platform.

In this study, I suggest a highly tunable, substrate-free, colloidal-quantum-dot-based PC laser employing colloidal quantum dots (CQDs) as gain material with a PC backbone. This building approach therefore, opens a door to integration of sub-micron scale laser to a very popular on-chip device platform. In the next section, CQDs and PC structures are briefly introduced for basic understanding of backgrounds. In order to exhibit unprecedented performance properties and new functionalities, types of CQDs and PC lattices are carefully chosen at the end of this chapter.

## 1.2 Alternative approach – colloidal quantum dot as a gain material

### 1.2.1 Colloidal quantum dots (CQDs)

This study employs colloidal quantum dots (CQDs) as optical gain material to solve the tunability and substrate issues that pointed out in the previous section. CQDs are simply spin-coated to form a deposited film. CQDs have advantages over epitaxially grown, common MQWs in many aspects. As shown in Fig 1-2-1, monodisperse CQDs can be chemically synthesized<sup>32, 33</sup> and therefore highly cost-effective. More importantly, their emission wavelengths are highly tunable due to quantum confinement effect of small physical diameter of individual CQD without changing its composing semiconductor materials. Introduction of the core-shell structure boosted up the quantum yield of such CQDs.<sup>34-36</sup>

### 1.2.2 Lasers based on colloidal quantum dots

Previous studies have found ways for lasing operation by incorporating CQDs into an appropriate cavity structure using CQDs on a certain type of resonant structure design. Figure 1-2-2 shows some of these previous works with “CQD gain and optical resonance-supporting structure” approach.

Random laser was reported, which used a simple groove of glass substrate to provide disordered structure for optical resonance.<sup>37</sup> This structure is manually prepared with diamond-tip scribe. This report was a primitive demonstration of CQD-incorporating laser device idea proving that densely-packed CQDs films can be source of optical gain appropriate for laser action. Even though this device

presented proof-of-concept device showing the resonance mode tuned at material (CdSe/ZnS CQDs) gain maximum, a random laser inherently has random optical confinement path in nature. Reported linewidth of the laser is quite broad ( $\sim 4$  nm) showing quadratic behavior in light-input versus light-output ( $L-L$ ) characteristic curve. I prefer an optical device with concrete principles of design on purpose to such a design depending on randomness.

A distributed feed-back (DFB) laser was reported with CdSe/CdS/Cd<sub>0.5</sub>Zn<sub>0.5</sub>S/ZnS CQD films as optical gain materials at  $\lambda \sim 650$  nm.<sup>38</sup> The CQD-DFB device structure utilized 250 nm-thick CQD films for optical gain over one-dimensional (1D) surface grating structure fabricated by nanoimprint lithography. In spite of DFB design, it showed DFB lasing operation by one-photon and two-photon absorption with  $20 \mu\text{m} \times 20 \mu\text{m}$  pumping beam-spot area.

Another distributed feed-back (DFB) laser was reported with CdSe/ZnCdS CQD gain films as optical gain materials, and for all three colors: red, green, and blue.<sup>39</sup> The CQD-DFB device structure also utilized (1D) surface grating structure for optical gain over broad area of device. Due to the nature of DFB design, cylindrical lens-focused, an elongated pumping beam-spot up to  $\sim 200 \mu\text{m}$  in length had to be used for proper optical pumping of the laser.

Vertical-cavity surface-emitting laser (VCSEL) was later introduced by the same group of researchers with CQD-DFB laser, which used the CdSe/ZnCdS CQD layer sandwiched between layers of external cavity structure.<sup>40</sup> In this study, eight pairs of quarter-wavelength SiO<sub>2</sub>/TiO<sub>2</sub> distributed Bragg reflector (DBR) were used for surrounding CQD layer. Thanks to the use of two DBRs, it achieves threshold  $\sim 60 \mu\text{J}/\text{cm}^2$ , which is lower than that of the CQD-DFB laser.

However, these previous studies require quite large optical pumping area, high threshold or complicated external cavity structure implantation. Therefore, the application of spin-coated CQDs for optical gain to a passive PC structure for optical resonance can be an efficient way not only because PCs provide small modal volume for resonance, but also because thresholds are reasonably low as already reviewed in previous section. CQD spin-coating process enables integration of the CQD-based PC light source onto on-chip devices with other passive optical components.

### 1.2.3 Selection and supply of CQDs

Highly-luminescent red-emitting CQDs used in the study are supplied by Samsung Advanced Institute of Technology. Spin-coating of CQDs on a pre-fabricated PC backbone is also conducted by co-workers in the same institute. Preparation of CQDs is briefly introduced in the appendix (See Appendix A), and major procedures for CQD synthesis and film deposition are provided in references.<sup>41, 42</sup>

Red-emitting CQDs were chosen, although they are able to be prepared in many colors, mainly because of fabrication factor of PC structure and applicability in the future. Considering the scale-law of PC structure, a relatively long wavelength emission can easily be supported, even though PCs have relatively large lattice constant of PC. In terms of fabrication, large lattice constant means facile fabrication in a few hundred nanometer scale. In addition, future use of the device would be maximized as a bio-material involved on-chip laser device when its wavelength is closer to red-to-infrared spectral region because of optical window of

bio-tissue.<sup>43</sup> Since the wavelength range from 650 nm to 1400 nm have low effective attenuation coefficient of skin, fat, and blood tissue, securing laser device for early 600 nm wavelength range is an important condition for bio-target imaging.



Figure 1-2-1 Colloidal quantum dots with different diameters, exhibiting various colors.<sup>35</sup>

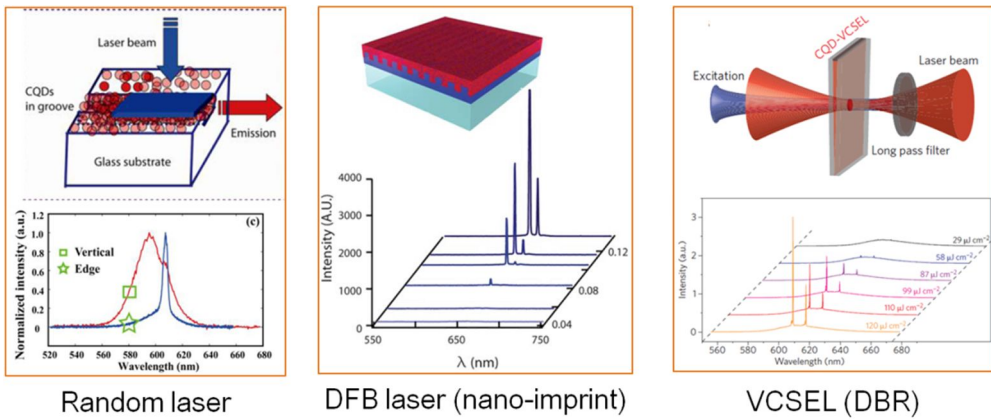


Figure 1-2-2 Various types of lasers built with QDs with different structures: random cavity, 1D surface grating, and vertical cavity<sup>37, 38, 40</sup>

## 1.2.4 Photonic crystals

Periodic distribution of index of refraction leads to unique photonic band structure. Figure 1-2-3 shows representations of three types of PC applications to a variety of PC structure and realized devices by various fabrication methods. Scanning electron microscope (SEM) images of optical devices with 1D, 2D, and 3D PCs with sub-micron periods are shown in Fig. 1-2-4; a distributed Bragg reflector, an InGaAsP-based band-edge laser, and an opal crystal, respectively.

Photonic crystals and electronic crystals (namely, crystalline solids) can be explained using elegant analogy. Forbidden photonic band-gap (PBG) and electronic energy band-gap, periodic dielectric function and periodic electronic potential, Maxwell and Schrodinger equations are all counterparts following such an analogy. Table 1-2-1 shows fundamental similarities between photonics and electronics. Figure 1-2-5 presents the similar properties of photonic and electronic crystals showing band structure with zone-folding. PBG and photonic band-edge (PBE) modes can be understood in terms of electronic band-gap and conduction-valence band model in solids.

Photonic band-gap (PBG) is a range of frequencies where light is forbidden to propagate through PC structure.<sup>44, 45</sup> Due to the fact that light propagation is forbidden into lateral slab waveguide, it is possible to construct useful optical devices in principles of the PBG, for example, optical cavities<sup>11, 46</sup> and waveguides.<sup>47</sup>  
<sup>48</sup> A PC cavity laser is an active device using a high Q optical cavity surrounded by PBG. A PC waveguide is a passive device, namely a photonic wire connecting components of photonic integrated-circuits, also using PBG effect keeping

electromagnetic waves from leaking out of optical path defined by PC pattern.

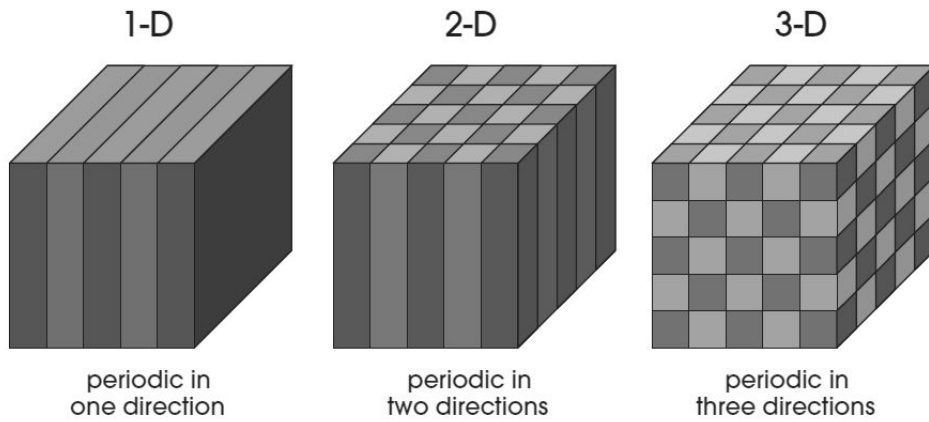


Figure 1-2-3 representations of 1D, 2D, and 3D PCs.<sup>45</sup>

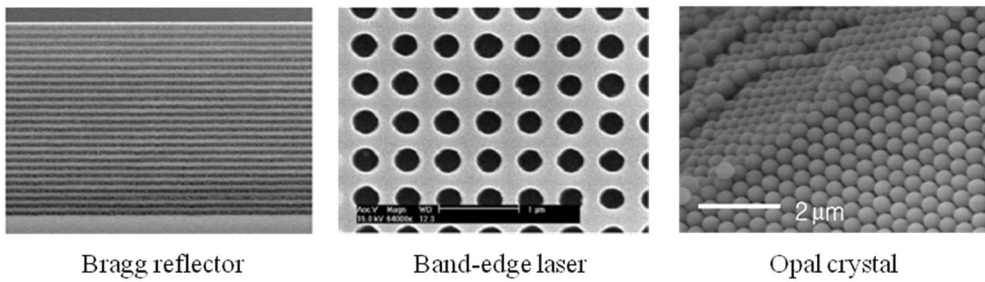


Figure 1-2-4 SEM images of examples of PCs with sub-micron periods

Electronic Crystal	Photonic Crystal
Periodic electronic potential	Periodic dielectric distribution
Electronic band-gap	Photonic band-gap
Schrodinger equation $\left[ -\frac{\hbar^2}{2m} \nabla^2 + V(\mathbf{r}) \right] \psi_E(\mathbf{r}) = E \psi_E(\mathbf{r})$	Maxwell equation $\nabla \times \frac{1}{\epsilon(\mathbf{r})} \nabla \times \mathbf{H}_\omega(\mathbf{r}) = \frac{\omega^2}{c^2} \mathbf{H}_\omega(\mathbf{r})$

Table 1-2-1 one-to-one correspondence between PCs and electronic crystals<sup>45</sup>

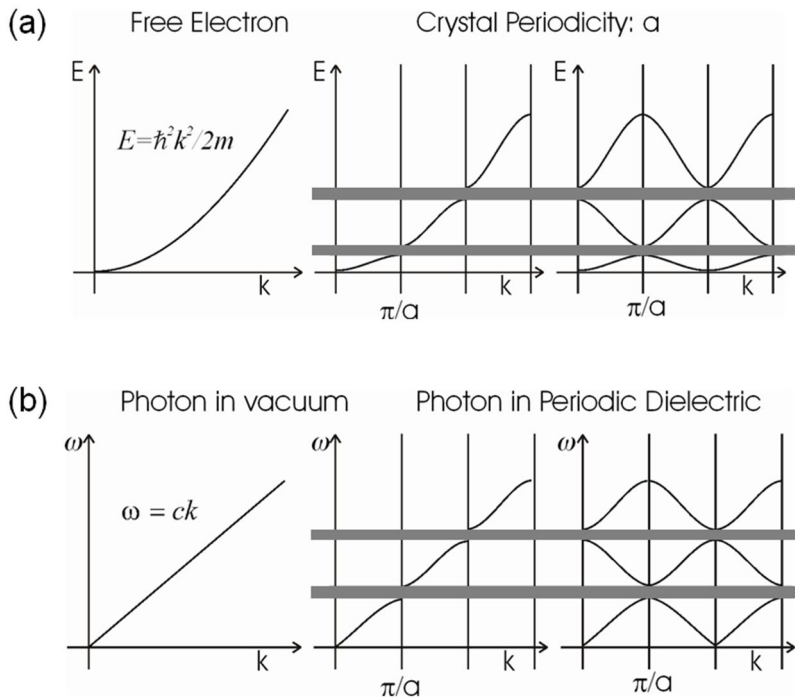


Figure 1-2-5 Dispersion relation between (a) momentum and energy of one electron in an electronic crystal, (b) frequency of electromagnetic fields and wave vector  $\mathbf{k}$  in a photonic crystal structure<sup>45</sup>

Photonic band-edge (PBE) modes also demonstrate novel and unique properties for PC-based optical devices. Group velocity of light at a PBE mode wavelength approaches zero where light experiences significantly stronger light-matter interaction.<sup>49, 50</sup> Photonic band-edge lasers are most well-developed PBE mode utilizing devices, in which emission wavelength of photons is tuned to the PBE modes providing enhanced optical gain, thus leading to lasing operation.<sup>29, 51-53</sup> In addition, PBE modes were used to design conditions for the enhancement of absorption efficiency of photovoltaic devices and light-absorbing phosphors for light-emitting devices.<sup>54-56</sup>

### 1.2.5 Selection of types of PC lattices

First of all, the PC structure using PBE modes is a better choice for easier fabrication and proof of concept CQD-PC laser. Other than one-dimensional (1D) DFB type, there are two choices for full PC laser architecture—PC cavity laser and PC band-edge laser. In case of PC cavity laser, a cavity must be defined in PC structure, which introduces at least one more step to fabrication process. The cavity part might be a source of non-uniformity or complication for CQD film spin-coating process. In addition, it is slightly more difficult to examine properties of PC cavity backbone prior to the CQD spin-coating process.

In contrast, PC band-edge laser does not require such a cavity design. Uniform air-hole perforation is possibly better for uniform spin-coating of CQD film. Therefore, it is natural to choose band-edge laser architecture for easier and faster proof of concept for CQD-PC laser.

Selection of PC lattice type is the next step. Two-dimensional (2D) triangular,

square, rectangular, and honeycomb lattices are available for selection because it is desirable to avoid similar 1D design. Triangular lattice is usually the choice of PC structure for PC cavity laser design due to higher air-hole density around a center cavity. Honeycomb lattice, which is a variation of triangular lattice, is a structure of choice for electrical injection to PC laser due to its high filling factor—honeycomb lattice lacks an air-hole in every two unit cells of triangular lattice, which leads to more material than triangular lattice.

Since a simple design for simple application is desirable, square lattice is the appropriate choice for CQD-PC laser. There is no need to choose rectangular lattice with two different lattice constants in x-, and y-axis of design, which only complicates the future modal analyses.

Thus, I decided to build CQD-PC 2D square lattice band-edge laser for this study. Figure 1-2-6 shows a schematic illustration of such a device. It is worth mentioning that CQD over-layer is naturally expected during the fabrication process. All numerical analyses should account for CQD over-layer for correct modeling of device.

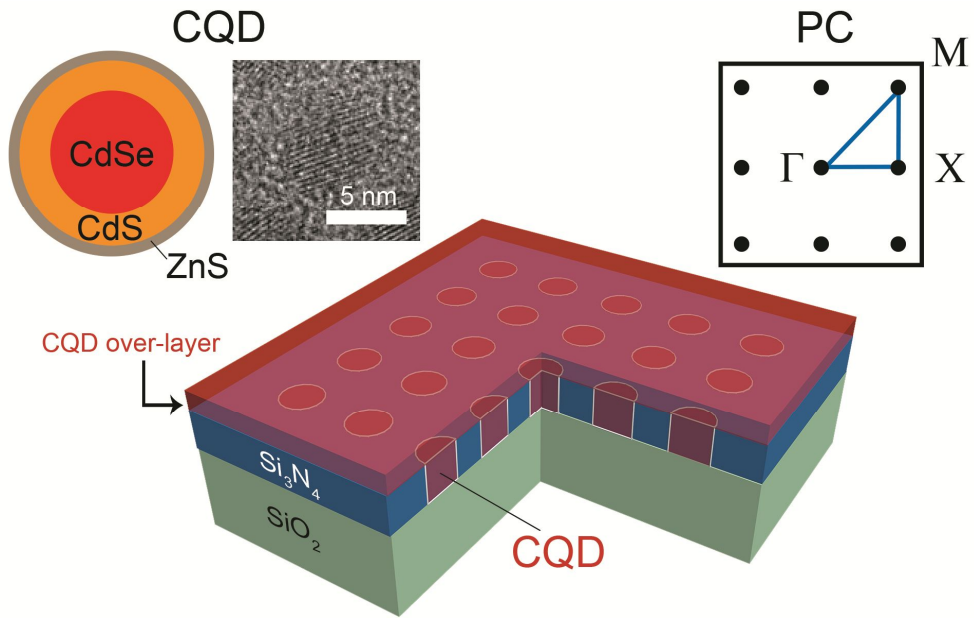


Figure 1-2-6 Schematic of CQD-PC band-edge laser structure. The Si<sub>3</sub>N<sub>4</sub> waveguide slab perforated with a square lattice array of air-holes serves a passive PC backbone on SiO<sub>2</sub>-cladding/Si-substrate. Spin-coated CQDs not only infiltrate the air-holes but also form a thin over-layer. Shown together are (left) a schematic structure as well as a transmission electron microscope image of the CdSe/CdS/ZnS core-shell-shell CQD and (right) the reciprocal lattice of square lattice PC with high symmetry points marked.

### 1.3 Summary and outline of the manuscript

I suggest a new concept of CQD-PC band-edge lasers to enhance functionality and compatibility for future on-chip applications. Two-dimensional square lattice type PC structure is modeled, fabricated, measured proving that a novel concept of the CQD-PC structure works.

In Chapter 2, photonic band structure of such device is investigated. Design principles and optical properties of PC structure are discussed by PWE and FDTD modeling in order to find a suitable symmetric point to use for proper lasing. Plus, modes are characterized in terms of FDTD method observing that PBE effect at M-point can be easily tuned for CQD gain bandwidth.

In Chapter 3, design of such a PC laser using CQD as a gain material is realized by a set of fabrication steps. Details of fabrication procedure considering actual engineering tolerance are to be discussed. CQD synthesis and spin-coating process is briefly introduced.

In Chapter 4, measurement results and discussion on CQD-PC laser performance is presented. Measurement setup and lasing features of devices are introduced and analyzed in accordance with predictions of FDTD numerical analysis, especially in terms of CQD over-layer thickness.

Finally, Chapter 5 concludes the dissertation with summary and future implication.

## References

1. A. Khan, "Semiconductor photonics: Laser diodes go green", *Nat. Photonics*, **3**, 432 (2009).
2. J.-Y. Kim, Y. Tak, J. Kim, H.-G. Hong, S. Chae, J. W. Lee, H. Choi, Y. Park, U. I. Chung, J.-R. Kim and J.-I. Shim, 2012.
3. A. Melton, B. Kucukgok, B. Wang, N. Dietz, N. Lu and I. Ferguson, MRS Proceedings, Cambridge Univ Press, 2013.
4. S. Nakamura and S. F. Chichibu, *Introduction to nitride semiconductor blue lasers and light emitting diodes*, (Taylor & Francis, 2000).
5. R. F. Oulton, V. J. Sorger, T. Zentgraf, R. M. Ma, C. Gladden, L. Dai, G. Bartal and X. Zhang, "Plasmon lasers at deep subwavelength scale", *Nature*, **461**, 629 (2009).
6. M. A. Noginov, G. Zhu, A. M. Belgrave, R. Bakker, V. M. Shalaev, E. E. Narimanov, S. Stout, E. Herz, T. Suteewong and U. Wiesner, "Demonstration of a spaser-based nanolaser", *Nature*, **460**, 1110 (2009).
7. R. M. Ma, R. F. Oulton, V. J. Sorger, G. Bartal and X. A. Zhang, "Room-temperature sub-diffraction-limited plasmon laser by total internal reflection", *Nat. Mater.*, **10**, 110 (2011).
8. W. Zhou, M. Dridi, J. Y. Suh, C. H. Kim, D. T. Co, M. R. Wasielewski, G. C. Schatz and T. W. Odom, "Lasing action in strongly coupled plasmonic nanocavity arrays", *Nat. Nanotechnol.*, **8**, 506 (2013).
9. S. Kim, J. Lee and H. Jeon, "Over 1 hour continuous-wave operation of photonic crystal lasers", *Opt. Express*, **19**, 1 (2010).

10. S. Kim, S. Kim, K. Hwang, H. Jeon and H. J. Kim, "Operation of Photonic Crystal Laser in Continuous-Wave Mode for 18 Hours", *Appl. Phys. Express*, **4**, 122101 (2011).
11. O. Painter, R. K. Lee, A. Scherer, A. Yariv, J. D. O'Brien, P. D. Dapkus and I. Kim, "Two-dimensional photonic band-gap defect mode laser", *Science*, **284**, 1819 (1999).
12. H. G. Park, S. H. Kim, S. H. Kwon, Y. G. Ju, J. K. Yang, J. H. Baek, S. B. Kim and Y. H. Lee, "Electrically driven single-cell photonic crystal laser", *Science*, **305**, 1444 (2004).
13. D. U. Kim, S. Kim, J. Lee, S. R. Jeon and H. Jeon, "Free-Standing GaN-Based Photonic Crystal Band-Edge Laser", *IEEE Photon. Technol. L.*, **23**, 1454 (2011).
14. S. Ahn, H. Kim, H. Jeon, J. R. Oh, Y. R. Do and H. J. Kim, "Two-Dimensional Hexagonal Lattice Photonic Crystal Band-Edge Laser Patterned by Nanosphere Lithography", *Appl. Phys. Express*, **5**, 042102 (2012).
15. M. Arita, S. Ishida, S. Kako, S. Iwamoto and Y. Arakawa, "AIN air-bridge photonic crystal nanocavities demonstrating high quality factor", *Appl. Phys. Lett.*, **91** (2007).
16. N. Carlsson, N. Ikeda, Y. Sugimoto, K. Asakawa, T. Takemori, Y. Katayama, N. Kawai and K. Inoue, "Design, nano-fabrication and analysis of near-infrared 2D photonic crystal air-bridge structures", *Opt. Quant. Electron.*, **34**, 123 (2002).
17. S. Chakravarty, P. Bhattacharya and Z. Mi, "Electrically injected quantum-dot photonic crystal microcavity light-emitting arrays with air-bridge contacts",

*IEEE Photon. Technol. L.*, **18**, 2665 (2006).

18. A. Chalcraft and D. M. Whittaker, "Modelling air-bridge photonic crystal defects by guided mode expansion", *Superlattice Microst.*, **41**, 425 (2007).
19. N. Ikeda, Y. Sugimoto, Y. Tanaka, K. Inoue, H. Oda, Y. Watanabe and K. Asakawa, "Studies on key nano-fabrication processes for GaAs-based air-bridge-type two-dimensional photonic-crystal slab waveguides", *Semicond. Sci. Tech.*, **22**, 149 (2007).
20. N. Kawai, K. Inoue, N. Carlsson, N. Ikeda, Y. Sugimoto, K. Asakawa and T. Takemori, "Confined band gap in an air-bridge type of two-dimensional AlGaAs photonic crystal", *Phys. Rev. Lett.*, **86**, 2289 (2001).
21. M. Luo and Q. H. Liu, "Enhancement of second-harmonic generation in an air-bridge photonic crystal slab: simulation by spectral element method", *J. Opt. Soc. Am. B*, **28**, 2879 (2011).
22. S. Nakayama, S. Iwamoto, S. Ishida, D. Bordel, E. Augendre, L. Clavelier and Y. Arakawa, "Enhancement of photoluminescence from germanium by utilizing air-bridge-type photonic crystal slab", *Physica E*, **42**, 2556 (2010).
23. Y. Sugimoto, N. Ikeda, N. Carlsson, K. Asakawa, N. Kawai and K. Inoue, "Theoretical and experimental investigation of straight defect waveguides in AlGaAs-based air-bridge-type two-dimensional photonic crystal slabs", *Appl. Phys. Lett.*, **79**, 4286 (2001).
24. Y. Sugimoto, N. Ikeda, N. Carlsson, K. Asakawa, N. Kawai and K. Inoue, "Light-propagation characteristics of Y-branch defect waveguides in AlGaAs-based air-bridge-type two-dimensional photonic crystal slabs", *Opt. Lett.*, **27**, 388 (2002).

25. Y. Sugimoto, N. Ikeda, N. Carlsson, K. Asakawa, N. Kawai and K. Inoue, "Experimental verification of guided modes in 60 degrees-bent defect waveguides in AlGaAs-based air-bridge-type two-dimensional photonic crystal slabs", *J. Appl. Phys.*, **91**, 3477 (2002).
26. J. Tian, S. Z. Han, B. Y. Cheng, Z. Y. Li, S. Feng, D. Z. Zhang and A. Z. Jin, "Two-dimensional silicon-based photonic crystal slab with partial air-bridge", *Acta Phys. Sin-Ch. Ed*, **54**, 1218 (2005).
27. Y. Watanabe, N. Ikeda, Y. Sugimoto, Y. Takata, Y. Kitagawa, A. Mizutani, N. Ozaki and K. Asakawa, "Topology optimization of waveguide bends with wide, flat bandwidth in air-bridge-type photonic crystal slabs", *J. Appl. Phys.*, **101** (2007).
28. Y. Watanabe, N. Yamamoto, K. Komori, H. Nakamura, Y. Sugimoto, Y. Tanaka, N. Ikeda, K. Asakawa and K. Inoue, "Simulation of group-velocity-dependent phase shift induced by refractive-index change in an air-bridge-type AlGaAs two-dimensional photonic crystal slab waveguide", *J. Opt. Soc. Am. B*, **21**, 1833 (2004).
29. S. Kim, S. Ahn, K. Min, S. Kim, H. Jeon, P. Regreny and C. Seassal, "Nano Stepping-Stone Laser", *Appl. Phys. Express*, **6**, 042703 (2013).
30. T. Yoshie, J. Vuckovic, A. Scherer, H. Chen and D. Deppe, "High quality two-dimensional photonic crystal slab cavities", *Appl. Phys. Lett.*, **79**, 4289 (2001).
31. E. M. Purcell, "Spontaneous Emission Probabilities at Radio Frequencies", *Phys. Rev.*, **69**, 681 (1946).
32. R. Rossetti, S. Nakahara and L. E. Brus, "Quantum Size Effects in the Redox Potentials, Resonance Raman-Spectra, and Electronic-Spectra of Cds Crystallites in Aqueous-Solution", *J. Chem. Phys.*, **79**, 1086 (1983).

33. C. B. Murray, D. J. Norris and M. G. Bawendi, "Synthesis and Characterization of Nearly Monodisperse Cde (E = S, Se, Te) Semiconductor Nanocrystallites", *J. Am. Chem. Soc.*, **115**, 8706 (1993).
34. M. A. Hines and P. Guyot-Sionnest, "Synthesis and characterization of strongly luminescing ZnS-Capped CdSe nanocrystals", *J. Phys. Chem-US*, **100**, 468 (1996).
35. B. O. Dabbousi, J. RodriguezViejo, F. V. Mikulec, J. R. Heine, H. Mattoussi, R. Ober, K. F. Jensen and M. G. Bawendi, "(CdSe)ZnS core-shell quantum dots: Synthesis and characterization of a size series of highly luminescent nanocrystallites", *J. Phys. Chem. B*, **101**, 9463 (1997).
36. C. B. Murray, C. R. Kagan and M. G. Bawendi, "Synthesis and characterization of monodisperse nanocrystals and close-packed nanocrystal assemblies", *Annu. Rev. Mater. Sci.*, **30**, 545 (2000).
37. Y. J. Chen, J. Herrnsdorf, B. Guilhabert, Y. F. Zhang, I. M. Watson, E. D. Gu, N. Laurand and M. D. Dawson, "Colloidal quantum dot random laser", *Opt. Express*, **19**, 2996 (2011).
38. R. Signorini, I. Fortunati, F. Todescato, S. Gardin, R. Bozio, J. J. Jasieniak, A. Martucci, G. Della Giustina, G. Brusatin and M. Guglielmi, "Facile production of up-converted quantum dot lasers", *Nanoscale*, **3**, 4109 (2011).
39. K. Roh, C. Dang, J. Lee, S. T. Chen, J. S. Steckel, S. Coe-Sullivan and A. Nurmikko, "Surface-emitting red, green, and blue colloidal quantum dot distributed feedback lasers", *Opt Express*, **22**, 18800 (2014).
40. C. Dang, J. Lee, C. Breen, J. S. Steckel, S. Coe-Sullivan and A. Nurmikko, "Red, green and blue lasing enabled by single-exciton gain in colloidal quantum dot

films", *Nat. Nanotechnol*, **7**, 335 (2012).

41. J. Lim, S. Jun, E. Jang, H. Baik, H. Kim and J. Cho, "Preparation of highly luminescent nanocrystals and their application to light-emitting diodes", *Adv. Mater.*, **19**, 1927 (2007).

42. K. S. Cho, E. K. Lee, W. J. Joo, E. Jang, T. H. Kim, S. J. Lee, S. J. Kwon, J. Y. Han, B. K. Kim, B. L. Choi and J. M. Kim, "High-performance crosslinked colloidal quantum-dot light-emitting diodes", *Nat. Photonics*, **3**, 341 (2009).

43. A. M. Smith, M. C. Mancini and S. M. Nie, "BIOIMAGING: Second window for in vivo imaging", *Nat. Nanotechnol*, **4**, 710 (2009).

44. E. Yablonovitch, "Inhibited Spontaneous Emission in Solid-State Physics and Electronics", *Phys. Rev. Lett.*, **58**, 2059 (1987).

45. J. D. Joannopoulos, *Photonic crystals : molding the flow of light*, (Princeton University Press, 2008).

46. H. Yokoyama, "Physics and Device Applications of Optical Microcavities", *Science*, **256**, 66 (1992).

47. C. J. M. Smith, H. Benisty, S. Olivier, M. Rattier, C. Weisbuch, T. F. Krauss, R. M. De La Rue, R. Houdre and U. Oesterle, "Low-loss channel waveguides with two-dimensional photonic crystal boundaries", *Appl. Phys. Lett.*, **77**, 2813 (2000).

48. Y. G. Roh, S. Yoon, H. Jeon, S. H. Han and Q. H. Park, "Experimental verification of cross talk reduction in photonic crystal waveguide crossings", *Appl. Phys. Lett.*, **85**, 3351 (2004).

49. S. John and T. Quang, "Spontaneous Emission near the Edge of a Photonic

Band-Gap", *Phys. Rev. A*, **50**, 1764 (1994).

50. T. Baba, "Slow light in photonic crystals", *Nat. Photonics*, **2**, 465 (2008).

51. J. P. Dowling, M. Scalora, M. J. Bloemer and C. M. Bowden, "The Photonic Band-Edge Laser - a New Approach to Gain Enhancement", *J. Appl. Phys.*, **75**, 1896 (1994).

52. S. H. Kwon, H. Y. Ryu, G. H. Kim, Y. H. Lee and S. B. Kim, "Photonic bandedge lasers in two-dimensional square-lattice photonic crystal slabs", *Appl. Phys. Lett.*, **83**, 3870 (2003).

53. S. H. Kwon, S. H. Kim, S. K. Kim and Y. H. Lee, "Small, low-loss heterogeneous photonic bandedge laser", *Opt. Express*, **12**, 5356 (2004).

54. D. Y. Zhou and R. Biswas, "Photonic crystal enhanced light-trapping in thin film solar cells", *J. Appl. Phys.*, **103** (2008).

55. Y. Park, E. Drouard, O. El Daif, X. Letartre, P. Viktorovitch, A. Fave, A. Kaminski, M. Lemitte and C. Seassal, "Absorption enhancement using photonic crystals for silicon thin film solar cells", *Opt. Express*, **17**, 14312 (2009).

56. C. M. Johnson, P. J. Reece and G. J. Conibeer, "Slow-light-enhanced upconversion for photovoltaic applications in one-dimensional photonic crystals", *Opt. Lett.*, **36**, 3990 (2011).

# Chapter 2

## Device Design and Numerical Analyses for CQD-PC Band-edge Lasers

### 2.1 Introduction

For realization of the concept of CQD-PC laser device developed in Chapter 1, CQD material characterization and deliberate choice of PBE modes are essential for fine-tuning of PBEs into CQDs gain bandwidth. Selection of CQDs and PBE modes dictates the intrinsic character of the laser. For band-edge lasers, usually,  $\Gamma$ -point design is preferred because light is emitted vertically to the out-of-plane direction, which is to be exact, the surface normal direction of the 2D PC device plane.<sup>1-3</sup>

It is necessary to design a device with firm construction of principles regarding device design and architecture. Optical properties of materials are briefly discussed prior to investigation using tools for numerical analyses. Next, starting with these principles, I explored possible combinations of PC structure and CQDs. Plane-wave expansion method and finite-domain time-difference methods will be introduced first, then CQD-PC design will be confirmed based on results of computation according to principles of design.

This chapter presents numerical analyses to determine PBE modes for CQD gain bandwidth tuning, and structural parameters. Photonic band structure and field profiles are provided as a result of computational simulations. The structural parameters for CQD-PC lasers are carefully selected before fabrication.

### 2.1.1 Plane-wave expansion method

Plane-wave expansion (PWE) method in electromagnetism is a computational algorithm solving Maxwell's equations. Especially in media with infinite periodicity, it is extremely useful tool for investigation of the photonic band structure of any lattice types of PCs. In particular, for 2D PC slab in 2D simulation, PWE method quickly returns modal solutions (eigenmode solutions) for describing photonic bands and fields profile.

Using PWE method, electric and magnetic field components are expanded in terms of Fourier components to solve Maxwell's equations along their reciprocal lattice vectors. Sets of differential equations are constructed to form an infinite matrix eigenvalue problem, which can be solved after proper approximation.<sup>4, 5</sup>

Commercially available computer software, BandSOLVE (RSoft Design Group), which simulation methods are based on the PWE method, to characterize modes found in a photonic band structure of the 2D PCs in Chapter 2. This method is used in order to quickly explore frequencies and field intensity profiles of band-edge modes in each symmetric points of 2D square PC structure in accordance with principles of CQD-PC laser device design. Results of analyses using this method provide approximate values of structural parameters—period, air-hole diameter, CQD over-layer thickness—for fabrication of the real device.

### 2.1.2 Finite-difference time-domain Method

Since PWE method was only used for 2D simulation of PC structure without considering its z-component, structural parameters found by PWE method only provide starting point of parameter sweeping, not the finalized exact value for fabrication. Finite-difference time-domain (FDTD) method is a widely used numerical analysis approach dividing space into discrete, mesh-like grids in which each of field components being analyzed in discrete time steps. Unlike PWE methods, most solutions of the time dependent Maxwell's equations can be solved exactly with no approximation in processes, and with no limitations in boundary conditions. The accuracy of solutions and computation time depend on the size of the grids and time steps.<sup>6</sup>

Lumerical FDTD Solutions (Lumerical Solutions, Inc.) was a commercial software package used for numerical analysis and device design to confirm photonic band structures, electric field profiles of each mode in the Chapter 2. This software package provides auto-meshing functions for efficient non-uniform mesh grid construction—compact mesh grid for complex parts of structure, but simple and relatively large mesh grid for simple parts of structure such substrate and free space.

Detailed analyses were conducted in 3D simulation for confirmation of exact values of structural parameters. The z-component ignored in PWE exploration is included in 3D FDTD simulation confirming photonic band structure and electric field profiles of each modal solution. The confirmed values of structural parameters and dimensions, tolerance factors are exactly followed in fabrication processes of the device.

## 2.2 Optical properties of materials for design

### 2.2.1 Indices of refraction: CQD film and Si<sub>3</sub>N<sub>4</sub> slab

Prior to discussion of photonic band structure, optical properties of CQD film and Si<sub>3</sub>N<sub>4</sub> must be known for exact modeling and tuning. In order to verify information on refractive index of red-emitting CQDs, complex index of refraction of a 70 nm-thick CQD film on a glass substrate was measured by ellipsometry at Samsung Advanced Institute of Technology as presented in Fig 2-2-1. According to Fig 2-2-1, the real part of index of refraction at the peak wavelength is  $n \sim 1.75$ . The indices of refraction are to be used for numerical analyses. Fig 2-2-2 also shows that Si<sub>3</sub>N<sub>4</sub> has refractive index  $n \sim 2.01$  at the peak wavelength.<sup>7</sup> Hence, the index contrast between high-index material (Si<sub>3</sub>N<sub>4</sub>) and low-index material (CQD) is  $\sim 0.3$ . Slab of Si<sub>3</sub>N<sub>4</sub> is known to be lossless dielectric material with no the imaginary part of complex index of refraction. CQD film also does not show any significant loss at emission wavelength range, where  $\kappa$  is less than  $10^{-3}$ . Absorption of CQD film is mainly at shorter wavelength region than  $\lambda \sim 600$  nm, which will be absorption bandwidth for optical pumping laser in further micro-photoluminescence measurement.

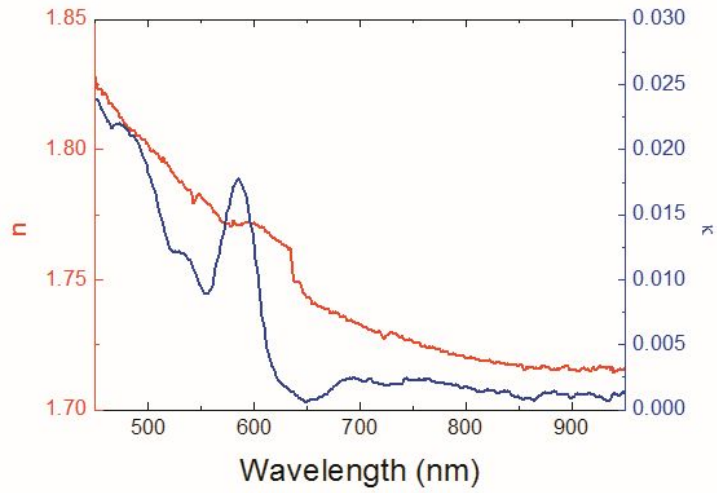


Figure 2-2-1 Measured index of refraction of CQD film. The real part of refractive index is  $n = 1.75$ . The thickness of measured layer is  $\sim 70$  nm.

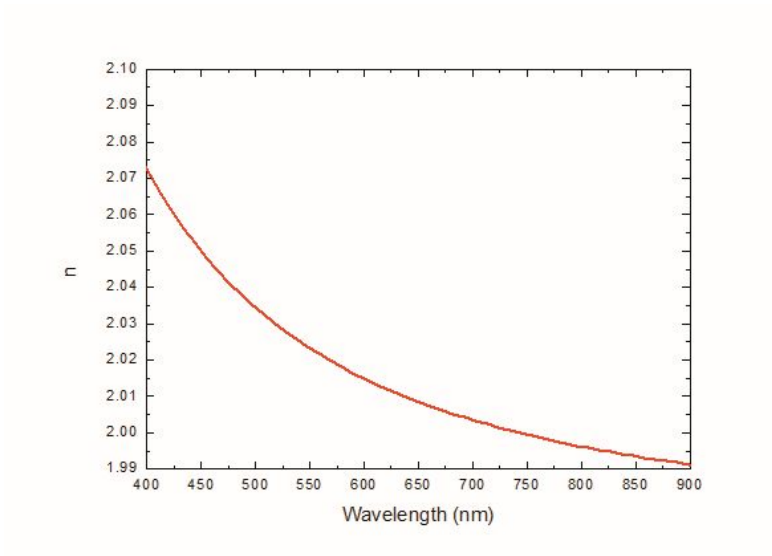


Figure 2-2-2 Index of refraction of  $\text{Si}_3\text{N}_4$ <sup>7</sup>

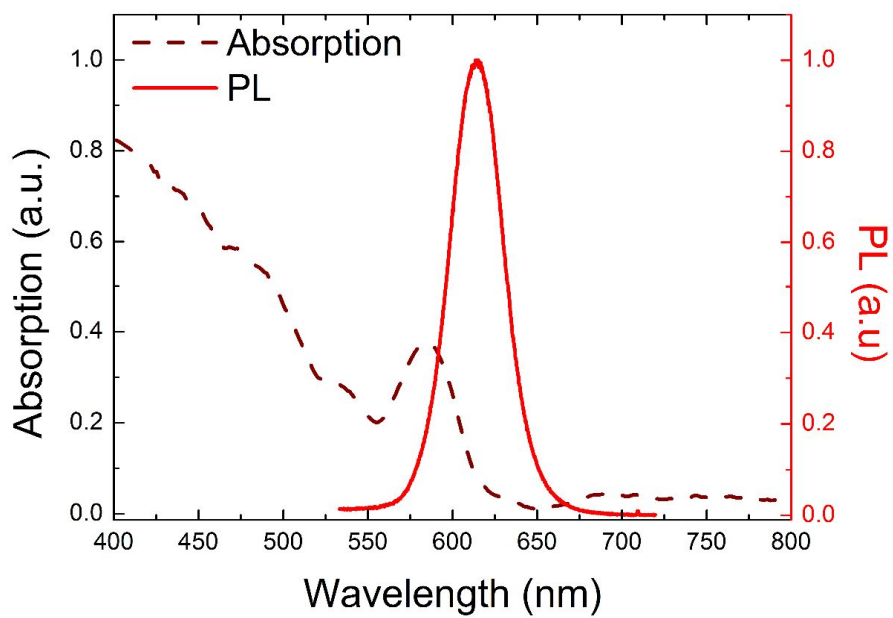


Figure 2-2-3 Measured photoluminescence and calculated absorption coefficient spectra of CQD film.

## 2.2.2 Optical properties of CQD film

The range of emission wavelength can be identified by a simple measurement of photoluminescence of CQD film. Figure 2-2-3 shows the photoluminescence data and absorption coefficient calculated from imaginary part of refractive index. CQD photoluminescence is the gain bandwidth of CQD film, and the peak wavelength is  $\lambda \sim 615$  nm with full-width half-maximum (FWHM)  $\sim 50$  nm. This bandwidth is the target of tuning for PBE modes, considering design principles and fabrication tolerance.

## 2.2.3 Thickness of Si<sub>3</sub>N<sub>4</sub> backbone slab waveguide

Generally, 2D PCs, whatever a type of lattice is, usually have slab waveguide that supports in-plane guided modes tuned to emission wavelength. Although this CQD-PC backbone design starts from asymmetric waveguide, a typical slab thickness for stable guided-modes is given as  $\sim \lambda/2n$ , which is approximately  $\sim 150$  nm in the case of Si<sub>3</sub>N<sub>4</sub>. It is merely a starting point to further discuss design of CQD-PC laser and its photonic band structure.

It is confirmed that stable guided mode is confined in the slab waveguide. As shown in Fig 2-2-4, to be specific, a simple stack of layers of different materials—Si, SiO<sub>2</sub>, Si<sub>3</sub>N<sub>4</sub>, CQD over-layer, and air from the bottom—are tested with another PWE method (CAMFR) at  $\lambda \sim 615$  nm. This simple examination of slab thicknesses only considered real parts of refractive indices. The x- component of electric field is strongly confined in CQD-Si<sub>3</sub>N<sub>4</sub> layer where the thickness of CQD layer is 100 nm, and the thickness of Si<sub>3</sub>N<sub>4</sub> slab is 150 nm. When using Si substrate, it is important to keep enough distance, preferably more than 500 nm, between Si and Si<sub>3</sub>N<sub>4</sub> slab

layer in order to avoid absorption loss to Si substrate.

The CQD-Si<sub>3</sub>N<sub>4</sub> layer effectively operates as a single guiding layer for the stack. Since the real part of refractive index of CQD is high enough, Si<sub>3</sub>N<sub>4</sub> is not the only slab region that electric field is confined to a guided mode. CQD layer can also be a part of guiding layer. It is important to note that a thick CQD over-layer might support more than one guided modes. Thus, thickness of CQD over-layer must be properly controlled in CQD film deposition process.

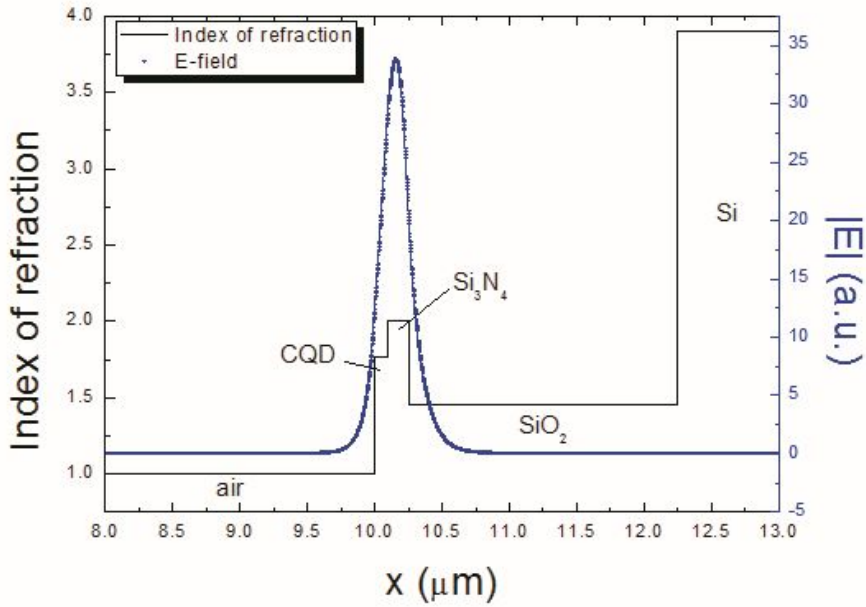


Figure 2-2-4 Index of refraction of CQD film. The real part of refractive index is  $n = 1.75$ . The thickness of measured layer is  $\sim 70$  nm.

## 2.3 Design of CQD-PC laser

### 2.3.1 Principles of CQD-PC laser design

Design of CQD-PC laser follows the principles as below:

- Find clear and distinct low index band-edge modes for maximizing CQDs' optical gain
- Use lower bands at high symmetric points for tuning of CQDs gain bandwidth for stable operation of modes
- Consider limits of fabrication methods for quality of device.

### 2.3.2 Photonic band structure of 2D square lattice PC by 2D PWE method

PWE method provides photonic band structures of an infinite PC structure. First, I started 2D PWE calculation with  $a = 200$  nm,  $r = 0.25a$  (filling factor 50%) gradually increasing period and adjusting air-hole diameter. Photonic bands of 2D PC using  $a = 220$  nm,  $2r = 140$  nm, with indices of refraction for CQDs in the air-hole and  $\text{Si}_3\text{N}_4$  that we confirmed in the previous section are calculated and shown in Fig. 2-3-1. The photonic band structure only provides information on typical band structure of 2D PC slab, however, design principles can be set up.

Since CQDs are the gain material with lower index than surrounding  $\text{Si}_3\text{N}_4$ , PBEs on any symmetric point should have distinct *low index band-edge* mode in

order to electric field to be overlapped properly as stated in the first principle above. Prominent symmetric points are  $\Gamma$ -, and M-point band-edges where the slope of bands clearly indicates that  $d\omega/dk \sim 0$ . Especially M-point has distinct *low index band-edge* modes as shown in Figure 2-3-1. I called the first and the second photonic band in the lower frequency region the *high index band-edge* (HIBE) and the third and the fourth band in the higher frequency region the *low index band-edge* (LIBE), which correspond to the “M<sub>1</sub>/M<sub>2</sub>” and “M<sub>3</sub>/M<sub>4</sub>” bands. Two LIBE modes clearly have electric fields focused at the center of air-holes with distinguishable mode spacing with respect to HIBE modes.

M-point has also an additional advantage over  $\Gamma$ -point in terms of tuning. Due to  $\lambda \sim 615$  nm center peak wavelength, PBE modes must be tuned to CQD gain bandwidth. Normalized frequencies of  $\Gamma$ -, and M-point band-edges imply that  $\Gamma$ -point band-edge modes have higher frequency, or shorter wavelength at  $\sim 440$  nm. M-point band-edges have lower frequency or longer wavelength at  $\sim 620$  nm, which is near the target emission wavelength of CQD. In turn, tuning CQD gain bandwidth to M-point band-edges can be easily achieved sweeping structural parameters. Structural parameters of M-point band-edge modes were verified by 3D FDTD method in the next section.

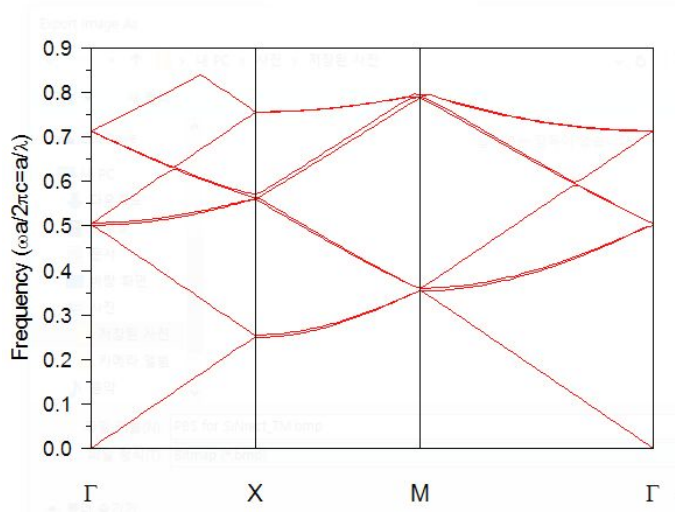


Figure 2-3-1 Typical photonic band structure of 2D square lattice PC. calculated by the PWE method.  $\Gamma$ - and M- point shows stable band-edge modes.

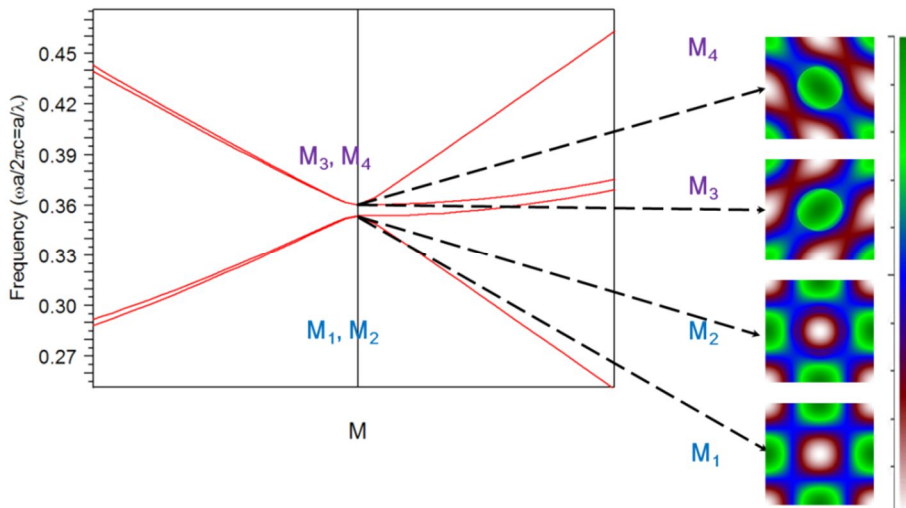


Figure 2-3-2 Photonic bands near the M-point of 2D PC. Insets show transverse electric field profiles in a unit cell of each band.

### 2.3.3 Photonic band structure of 2D square lattice PC by 3D FDTD method

It is worth a note that CQDs are assumed not only to infiltrate the air-holes but also to form a residual over-layer on top of the entire device, which is inevitable due to the nature of CQD film deposition by spin-coating. When modeling integral CQD-PC structure, this over-layer must be taken into account for 3D FDTD analyses because residual over-layer of CQD also becomes a part of PC slab waveguide.

Figure 2-3-3a shows the examined M-point band-edge modes for the transverse-electric (TE) polarization with 3D FDTD method. The lattice constant and air-hole diameter of the 2D PC are  $a = 255$  nm and  $2r = 140$  nm, respectively, while the waveguide structure is assumed to consist of a  $\text{Si}_3\text{N}_4$  slab ( $n_{\text{Si}_3\text{N}_4} = 2.01$ ;  $t_{\text{Si}_3\text{N}_4} = 140$  nm) and a CQD over-layer ( $n_{\text{CQD}} = 1.75$ ;  $t_{\text{CQD}} = 100$  nm), which is sandwiched between the claddings of a fused silica ( $n_{\text{SiO}_2} = 1.45$ ) in the bottom and the air ( $n_{\text{air}} = 1$ ) in the above. At the M-point that we choose for laser resonance, there are total four band-edge modes:  $M_1$ ,  $M_2$ ,  $M_3$ , and  $M_4$ , which are very similar to mode features according to PWE analyses in the previous section—Fig. 2-3-3b.

Figure 2-3-3c is a mode spectrum simulated by the same FDTD method but at a single symmetric point, presenting all the M-point band-edge modes. It should be noted that two LIBE modes,  $M_3$  and  $M_4$  are perfectly degenerate modes in energy so that they appeared to be merged into a single peak in the spectrum. Shown as the insets are the transverse electric field intensity profile ( $E_t^2 \equiv E_x^2 + E_y^2$ ) of two band-edge modes, representing  $M_2$  and  $M_3$ , respectively. The profiles of modes,  $M_1$  and  $M_4$  are not shown because  $M_1$  is very similar to that of  $M_2$ , while  $M_3$  and  $M_4$  are

identical except for the mode orientation rotated by  $90^\circ$ . It should also be noted that the modal intensity is concentrated in the dielectric region for  $M_2$  and in the air-hole filled with CQDs for  $M_3$ , which is consistent with the HIBE and LIBE, respectively. Figure 2-3-4 shows features of transverse electric field intensity profiles of each mode at M-point.

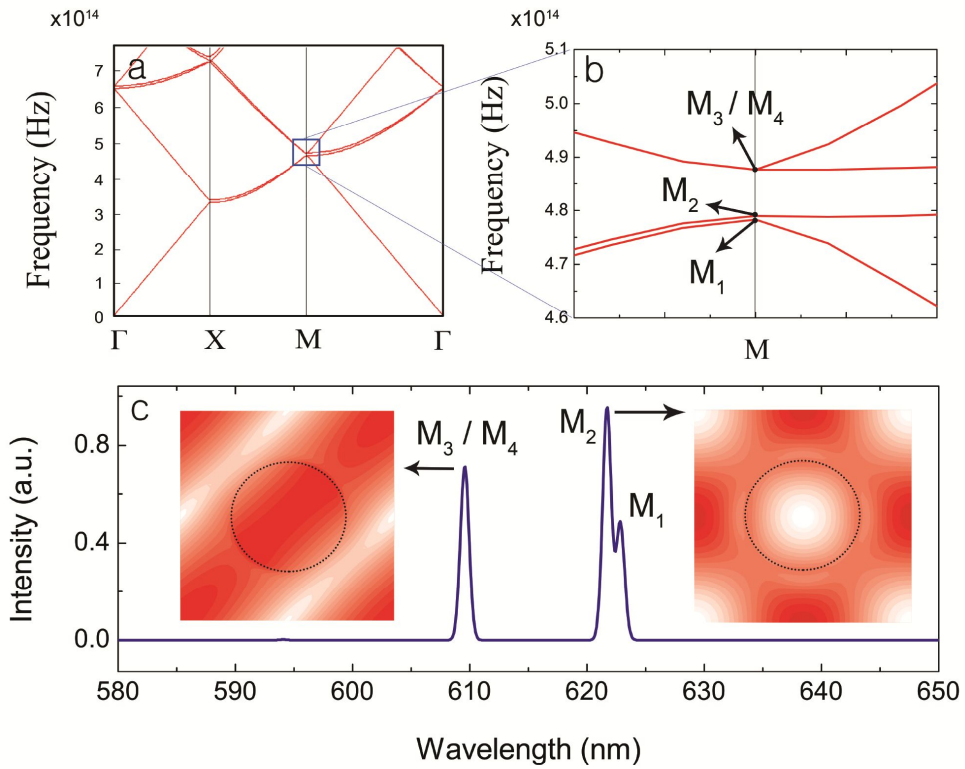


Figure 2-3-3 Photonic band structure and M-point band-edge mode properties of the 2D square lattice CQD-PC structure. (a)(b) Photonic band structure calculated by 3D FDTD: (a) overall and (b) near the M-point band-edges. (c) Resonant mode spectrum calculated for the M-point band-edges, exhibiting two HIBE modes ( $M_1$  and  $M_2$ ) at  $\lambda \sim 622$  nm and two degenerate LIBE modes ( $M_3$  and  $M_4$ ) at  $\lambda \sim 610$  nm. The insets display the band-edge mode profiles (transverse E-field intensity) for  $M_2$  and  $M_3/M_4$ , also calculated by 3D FDTD.

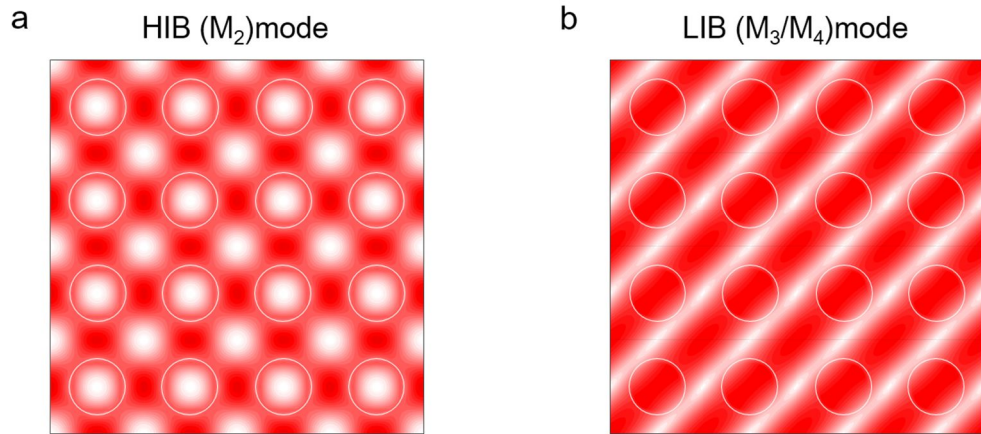


Figure 2-3-4 Transverse electric field intensity profiles of M-point band-edge modes properties of the 2D square lattice CQD-PC structure. (a) an HIBE mode:  $M_2$ (b)two degenerate LIBE modes:  $M_3$  and  $M_4$

## 2.4 Summary

In this chapter, the design of CQD-PC laser is finalized using 2D PWE and 3D FDTD as design tools for numerical analyses—the lattice constant  $a = 255$  nm and air-hole diameter  $2r = 140$  nm into Si<sub>3</sub>N<sub>4</sub>slab waveguide ( $n_{\text{Si}_3\text{N}_4} = 2.01$ ;  $t_{\text{Si}_3\text{N}_4} = 140$  nm) including CQD over-layer ( $n_{\text{CQD}} = 1.75$ ;  $t_{\text{CQD}} = 100$  nm).

The 2D PWE methods was a powerful tool for an early-stage exploration because it quickly returned information of designed photonic band structure and field profile of a certain mode. This process determined appropriate range of sweeping structural parameters for device design and the following PBE modes.

Having decided PBE modes and a type of CQD, it was moved on to the next step—3D FDTD simulation for further verification of parameters. Since the 2D PWE method, despite fast outcome, only accounted for in-plane  $k$  vector components for calculation, 3D FDTD should be performed to verify if PC have identical, or at least similar band structure and the PBE modes taking into account the  $k_z$  component. The 3D FDTD simulation finalized structural parameters above.

## References

1. Y. Park, S. Kim, C. Moon, H. Jeon and H. J. Kim, "Butt-end fiber coupling to a surface-emitting Gamma-point photonic crystal band edge laser", *Appl. Phys. Lett.*, **90**, 171115 (2007).
2. D. U. Kim, S. Kim, J. Lee, S. R. Jeon and H. Jeon, "Free-Standing GaN-Based Photonic Crystal Band-Edge Laser", *IEEE Photon. Technol. Lett.*, **23**, 1454 (2011).
3. S. Ahn, H. Kim, H. Jeon, J. R. Oh, Y. R. Do and H. J. Kim, "Two-Dimensional Hexagonal Lattice Photonic Crystal Band-Edge Laser Patterned by Nanosphere Lithography", *Appl. Phys. Express*, **5**, 042102 (2012).
4. K. M. Ho, C. T. Chan and C. M. Soukoulis, "Existence of a Photonic Gap in Periodic Dielectric Structures", *Phys. Rev. Lett.*, **65**, 3152 (1990).
5. R. D. Meade, A. M. Rappe, K. D. Brommer, J. D. Joannopoulos and O. L. Alerhand, "Accurate Theoretical-Analysis of Photonic Band-Gap Materials", *Phys Rev B*, **48**, 8434 (1993).
6. K. S. Yee, "Numerical Solution of Initial Boundary Value Problems Involving Maxwells Equations in Isotropic Media", *IEEE T Antenn. Propag.*, **Ap14**, 302 (1966).
7. H. R. Philipp, "Optical Properties of Silicon-Nitride", *J. Electrochem. Soc.*, **120**, 295 (1973).

# Chapter 3

## Fabrication of CQD-PC Band-edge

## Lasers

### 3.1 Introduction

This chapter deals with methods and equipment to fabricate devices realizing the design explored in Chapter 2. The CQD-PC band-edge lasers were fabricated by following consecutive processes. The fabrication processes consisted of two major steps: passive PC backbone fabrication and CQD spin-coating for filling air-holes. Figure xx shows the chain of fabrication processes except CQD synthesis. The core-shell-shell CQDs of CdSe/CdS/ZnS were synthesized based on the following publications.<sup>1,2</sup>

A variety of patterning methods are available to construct passive PC backbone, Table 3-1-1 shows various types of lithography techniques for patterning—electron beam lithography, photo-lithography, and laser holographic lithography (LHL). Because CQD-PC band-edge lasers are sensitive to quality of fabricated air-hole features, e-beam lithography have been a choice of patterning due to very high spatial resolution. However, it is noteworthy to mention that, for large areas in sub-micron scale, LHL is the prominent method that be used for cost-effective, large-area fabrication.<sup>3, 4</sup> This method was utilized as an additional tool for sample fabrication, which is explained in the section 3.3.

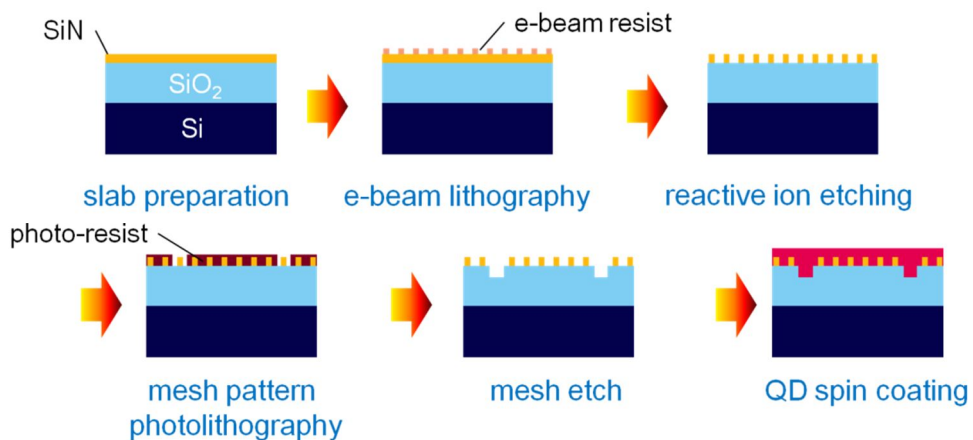


Figure 3-1-1 Fabrication processes of CQD-PC band-edge lasers.

	<b>E-beam lithography</b>	<b>Photo-lithography</b>	<b>Laser Holographic lithography</b>
Cost	high	high	low
Throughput	low	high	high
Large-area	X	O	O
Mask	O	O	X
Minimum feature size	~ 10 nm	~ 5 μm	~ 100 nm
Flexibility	O	O	X (periodic only)

Table 3-1-1 Comparison between three common lithography methods<sup>5</sup>

## 3.2 Fabrication processes

### 3.2.1 PC backbone fabrication

For fabrication of PC backbone, a 140-nm-thick  $\text{Si}_3\text{N}_4$  slab was deposited by plasma-enhanced chemical-vapor deposition (PECVD) on top of a thick  $\text{SiO}_2$  cladding layer on Si substrate. In order to isolate  $\text{Si}_3\text{N}_4$  slab waveguide using the  $\text{SiO}_2$  layer as the bottom cladding of the layers of  $\text{SiO}_2$  and  $\text{Si}_3\text{N}_4$  were sequentially deposited on Si substrate for 30 minutes and 6 minutes, respectively without venting the chamber.<sup>1,2</sup>

A square-lattice 2D air-hole array was patterned by electron-beam lithography. A positive electron-beam resist (ZEP520A) was applied by spin-coating onto the  $\text{Si}_3\text{N}_4$  surface at 4,000 rpm for 40 s to form a 200-nm-thick resist layer. Sequentially baked at 190°C for 2 min, and subjected to electron beam exposure to generate 2D square lattice PC pattern in an electron beam lithography system (JEOL JBX-6300FS at 100 keV electron acceleration voltage and 1 nA current). After developing the exposed resist using ZED-N50 for 5 min, a 2D square lattice was defined on the resist film.

The applied pattern is generated by Cadence Virtuoso Layout Suite (Cadence Design Systems, Inc.) in GDSII format. In order to compensate expected enlargement of air-hole diameter during the fabrication process, the original air-hole diameter is determined to be  $r = 0.13a$ . Devices were patterned in  $6 \times 6$  PC array form, which have different air-hole diameter by the dose of e-beam exposure. In order to ensure device operation, considering theoretical uncertainty as well as engineering tolerance during the fabrication process, the air-hole diameter is intentionally varied ( $2r = 120\text{-}150$  nm).

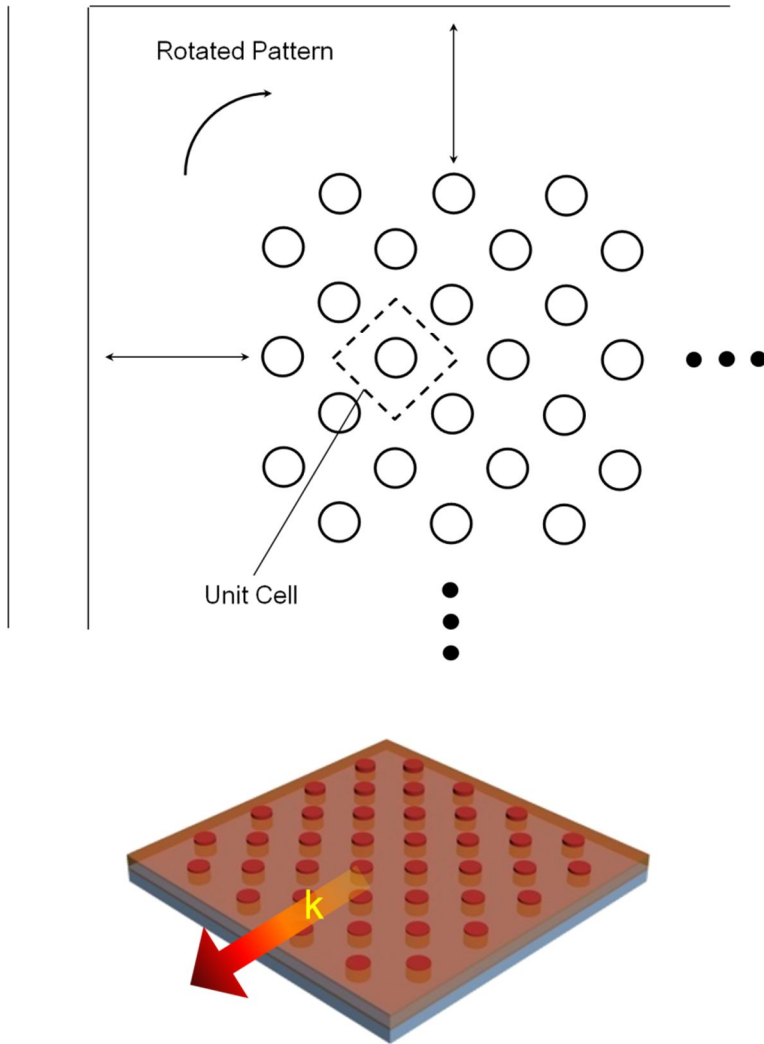


Figure 3-2-1 2D PC pattern cluster on a  $\text{Si}_3\text{N}_4/\text{SiO}_2/\text{Si}$  substrate rotated  $45^\circ$  to maintain stable electric field distribution of the M-point PBE modes. The schematic representation of device (above) shows unit cell of 2D PC and part of mesh grid line. The 3D representation (below) depicts an ideal device emitting light to  $k_{\parallel} = (1, 1)$  direction with no CQD over-layer on top.

The 2D square lattice PC cluster design was intentionally rotated by  $45^\circ$  with respect to the side of mesh grid line and an edge of PC cluster, and accordingly to the mesh grid as depicted in Fig. 3-2-1 so that the light emitting from the M-point band-edge modes be scattered out in the in-plane directions along the mesh grid. Since the uncertainty of which M-point mode be selected for lasing, the design must take into account that lasing of any mode experiences identical propagation length to the mesh grid for scattering, maintaining stable field distribution of M-point modes. so that there is no preference of a particular mode for data collection during subsequent measurement session.

The PC pattern formed on the resist layer was transferred to the underlying  $\text{Si}_3\text{N}_4$  layer by reactive-ion etching (RIE), completing a full  $\text{Si}_3\text{N}_4$  PC slab on top of the  $\text{SiO}_2$  cladding layer. The e-beam resist pattern was transferred to the underlying  $\text{Si}_3\text{N}_4$  layer using  $\text{CF}_4$ -based RIE ( $\text{CF}_4 : \text{O}_2 = 40 : 2$  in sccm, 100W RF power, 42 mTorr) for 1 min 40 sec. Rate of RIE was 1.5 nm/sec. at the time of run. The tech time is set to include slight over-etch of  $\text{Si}_3\text{N}_4$  layer. The e-beam resist was removed by dipping the samples in piranha solution ( $\text{H}_2\text{SO}_4 : \text{H}_2\text{O}_2 = 5 : 1$ ) for 3 min.

For easy identification of individual PC pattern and scattering of laser light off from device surface, a mesh grid was facilitated to the fabricated  $\text{Si}_3\text{N}_4$  PC backbone structure by photolithography as also depicted in Fig 3-2-1. Since the RIE conditions above also works for  $\text{SiO}_2$  cladding layer etching with only different etch rate from  $\text{Si}_3\text{N}_4$  layer, the same recipe was used for etching of the mesh grid pattern. Subsequent photo-resist removal was performed, again in the same piranha solution as before, which completes the PC backbone fabrication process.

Figure 3-2-2 shows an optical microscope image taken for the entire  $6 \times 6$  PC array with the mesh grid in-between, while Fig. 3-2-2b is an amplified image of the

50  $\mu\text{m} \times 50 \mu\text{m}$  PC pattern. Figure 3-2-2c and 2d are scanning electron microscopy (SEM) images of the  $\text{Si}_3\text{N}_4$  PC backbone in two different magnifications, exhibiting clean and uniform circular air-holes.

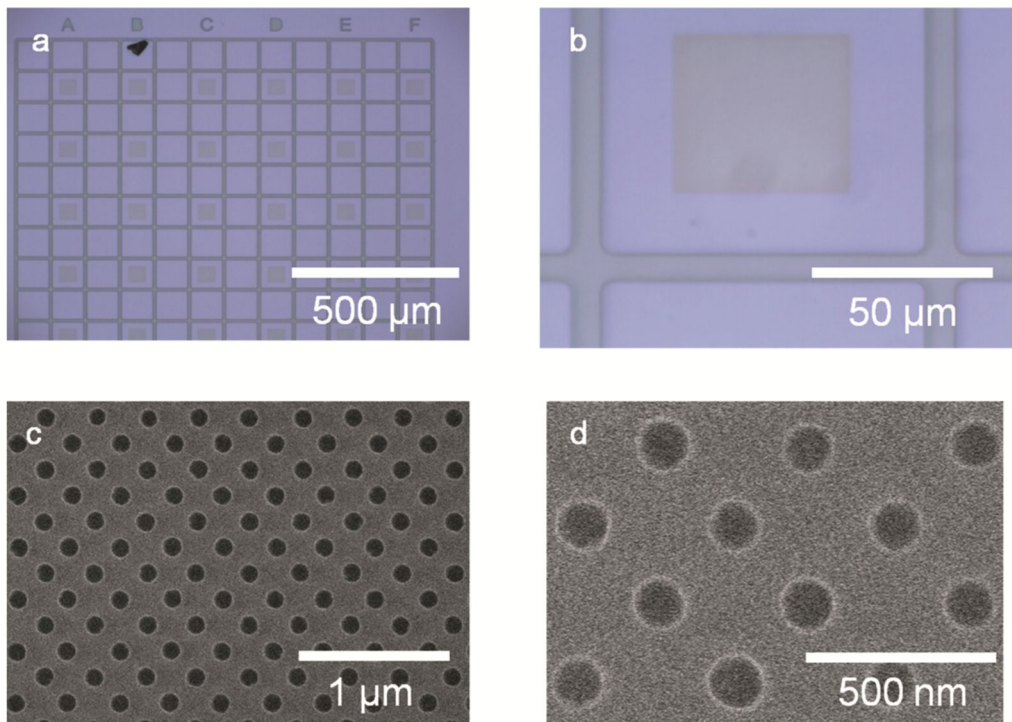


Figure 3-2-2 Images of fabricated CQD-PC laser devices. (a)(b) Optical microscope images of fabricated  $\text{Si}_3\text{N}_4$  PC backbone with the mesh grid pattern for device identification. (c)(d) SEM images of the fabricated  $\text{Si}_3\text{N}_4$  PC backbone.

### 3.2.2 CQD spin-coating

For CQD spin-coating after completing the fabrication of the passive  $\text{Si}_3\text{N}_4$  PC backbone, highly luminescent red-emitting CdSe-based CQDs were spin-coated in Samsung Advanced Institute of Technology.

In an ideal device, CQDs are supposed to fill the air-holes only with no over-layer on top of the PC slab as depicted in the 3D representation of Fig 3-2-1, which would then ensure lasing action only at the low index band-edge mode. In a real-world application, however, a CQD over-layer is inevitably formed on the entire PC backbone structure after spin-coating process. The CQD over-layer thickness depends on details of the CQD coating conditions: spinning speed and the solvent (cyclohexane) concentration.

Thin nominal thickness of CQD cannot provide sufficient amount of CQDs to cover all area of  $\text{Si}_3\text{N}_4$  PC backbone. If CQD over-layer is coated with too thin layer of CQDs, as shown in Fig 3-2-3, overall amount of CQDs are insufficient to cover all area of  $\text{Si}_3\text{N}_4$  PC backbone lacking optical gain sufficient to sustain stable lasing operation. The sample in Fig 3-2-3 is used for CQD spin-coating testing for nominal thickness  $\sim 30$  nm expecting almost “ideal device.” However, it definitely shows voids without CQDs that failing to fill air-holes of  $\text{Si}_3\text{N}_4$  PC backbone due to the lack of CQDs. On the contrary, if CQD over-layer is too thick, the existence of the CQD over-layer in reality might prevent CQD-PC device from lasing not only at the low index band-edge mode but also at the high index band-edge mode. It is required to apply thick layers of CQD despite of such risks to consider.

For proper CQD film deposition, CQDs were spin-coated to have  $\sim 80$  nm thickness so as to provide sufficient amount of CQDs into air-holes. When observed

after CQD spin-coating with scanning electron microscope (SEM), no PC pattern was visually confirmed as shown in Fig 3-2-4. Small dots shown on CQD over-layer are not the air-holes of 2D PC, but they are non-uniform clustering of CQDs. Even though the Fig 3-2-4 is a tilted view of CQD-PC device, the thickness of CQD over-layer appears to be more than  $\sim 100$  nm at least.

To confirm coverage of CQDs over air-holes of 2D PC backbone, surface of CQD over-layer was intentionally scratched as shown in Fig 3-2-5, revealing some of the air-holes underneath CQD over-layer. According to Fig 3-2-5b, it is clearly confirmed that the air-holes are completely filled with the CQDs with no sign of air void.

Further discussion on CQD over-layer thickness will be discussed later in Chapter 4.

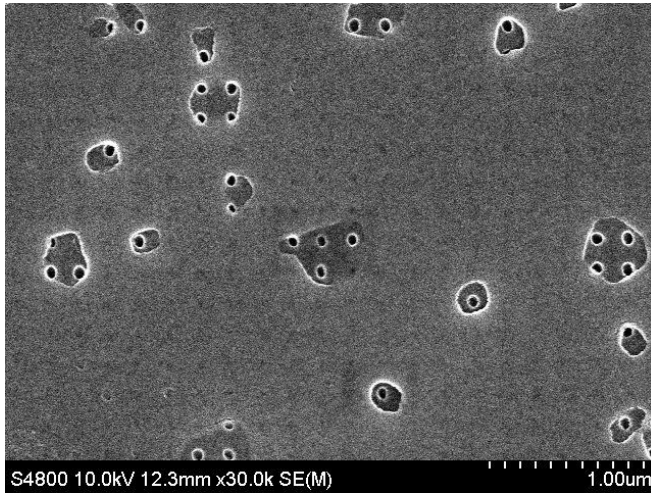


Figure 3-2-3 An SEM image of prototype testing sample. CQD spin-coating left CQD over-layer with void area (nominal thickness  $\sim 30$  nm) above PC cluster.

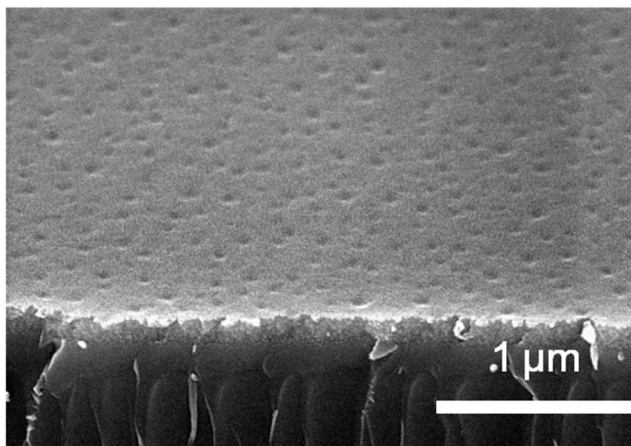


Figure 3-2-4 An SEM image of thick CQD over-layer above PC cluster

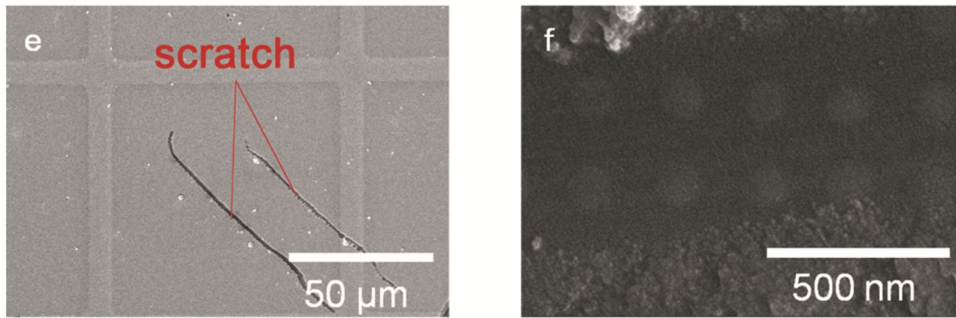


Figure 3-2-5 SEM images of CQD-PC device after CQD spin-coating for  $\sim 80$  nm nominal thickness (a) CQD over-layer scratched intentionally (b) confirmed CQD filling into the air-holes

### 3.3 Devices fabricated by laser holographic lithography

Laser holographic lithography (LHL) is an effective method for large-area patterning in sub-micron length scale with high throughput. Here in this study, the LHL was expected to provide profound samples that do not require a location-specific optical pumping due to the “pattern all-over” properties of the method. Holographically fabricated devices reported successful lasing operations in various researches.<sup>6</sup>

Standard operating principles of LHL method is particularly similar to those of optical interferometer. LHL method here in this study, shown in Fig. 3-3-1(a), used UV laser for light source with Lloyd’s mirror sample holder setup.<sup>4</sup> Electromagnetic waves emitted from a 266 nm diode-pumped solid-state (DPSS) laser are expanded by an objective lens, almost becoming planar waves near the mirror stage. Two coherent, planar light waves, one directly from the objective lens and the other reflected from the mirror generates interference pattern as can be seen in Fir. 3-3-1(b). Photo-resist (PR) pattern is generated in accordance with the periodic, intensity-varying, interference pattern of incident light after post-exposure process. The period of the periodic pattern is given by

$$\Lambda(\text{Period}) = \frac{\lambda}{2\sin\theta}$$

, where  $\lambda$  is the laser wavelength (= 266 nm) and  $\theta$  is the angle of rotation of the sample stage.

For fabrication of PC backbone, a 140-nm-thick  $\text{Si}_3\text{N}_4$  slab was deposited by plasma-enhanced chemical-vapor deposition (PECVD) on top of a quartz( $\text{SiO}_2$ ) substrate. This time, it was not necessary to isolate  $\text{Si}_3\text{N}_4$ slab waveguide from Si.

No sequential runs of PECVD were required. PECVD was conducted for 6 min. to deposit ~ 140 nm layer.

A square-lattice 2D air-hole array was patterned by double-exposure-LHL method. Double exposure technique is a sequential exposure to light source. After an initial exposure, the sample was rotated 90° and exposed again to light source. The exposure time was 32 seconds. A negative photo-resist (AZ nLOF 2070) was applied by spin-coating onto the Si<sub>3</sub>N<sub>4</sub> surface at 4,000 rpm for 40 seconds to form an approximately 300-nm-thick PR layer. Sequentially baked at 110°C for 1 min, and subjected to double exposure to generate 2D square lattice PC pattern. After the double exposure process, samples were baked at 110°C for 1 min again for negative tone image-reversal. Developing the exposed resist using AZ 300 MIF for 1 min, a 2D square lattice with air-holes pattern was defined on the resist film.

An identical RIE and cleaning process were followed to complete Si<sub>3</sub>N<sub>4</sub> backbone structure on a quartz substrate. No mesh grid was defined this time. Figure 3-3-2 shows the completed Si<sub>3</sub>N<sub>4</sub> PC backbone.

Apparently, the LHL-fabricated Si<sub>3</sub>N<sub>4</sub>PC backbone lacks uniformity of PC air-holes due to very short period of PC and relatively low sensitivity of PR. Compared to SEM images of Si<sub>3</sub>N<sub>4</sub>PC backbone fabricated by e-beam lithography, the quality of fabrication is not satisfying and definitely not enough to use as PC backbone for a laser device. It is expected to mature with further optimization, however, samples fabricated by LHL can be utilized for analyzing quality of spin-coated CQD film in the upcoming discussion in Chapter 4.

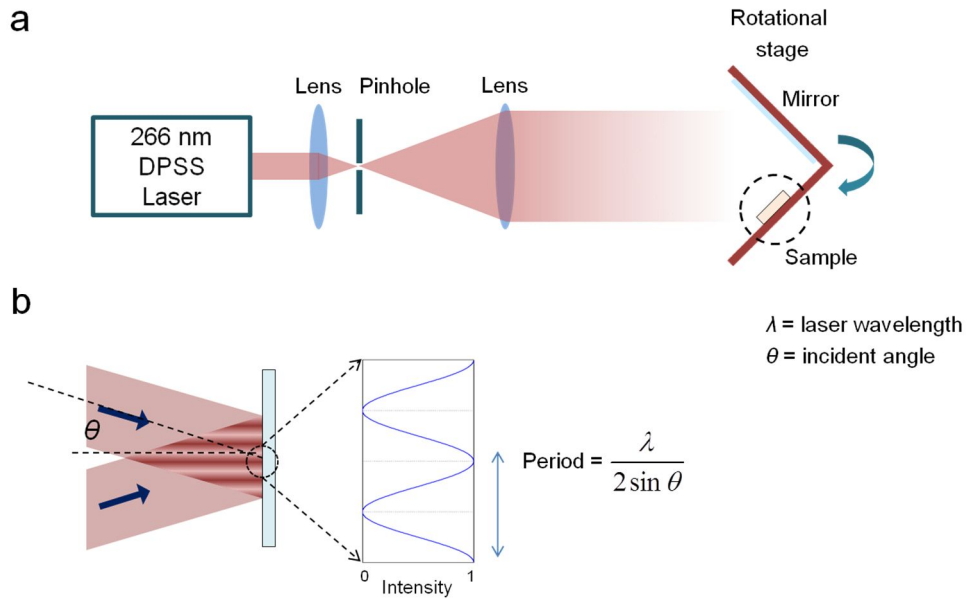


Figure 3-3-1(a) A schematic diagram of laser holographic lithography setup using 266 nm DPSS laser as a light source. (b) Interference pattern consisting of a periodic series of fringes representing intensity maxima and minima.<sup>5</sup>

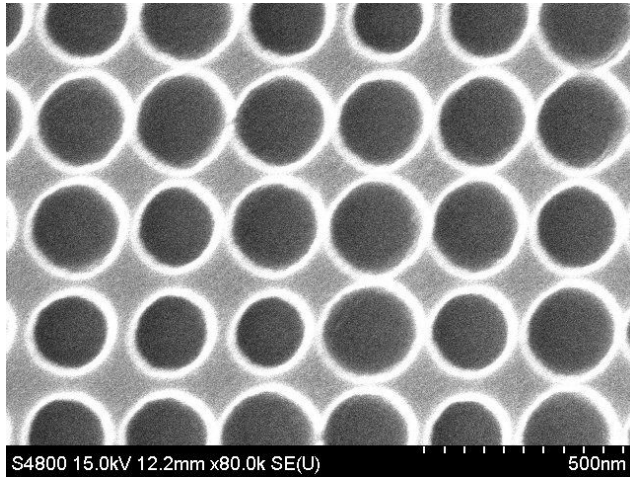


Figure 3-3-2 An SEM image of  $\text{Si}_3\text{N}_4$  PC backbone fabricated by LHL. Uniformity of air-holes was not up to the level of fabrication quality required to operate as a laser-mode supporting device backbone structure.

### 3.4 Summary

$\text{Si}_3\text{N}_4$  PC backbone for CQD-PC band-edge laser has been realized by sophisticated nano-fabrication technology. CQD spin-coating processes were also tested with varying concentration of solvent.

The samples of CQD-PC laser patterned by e-beam lithography technique on an asymmetric slab waveguide turned out to have profound quality for laser measurement. SEM images of  $\text{Si}_3\text{N}_4$  PC backbone before and after the CQD spin-coating showed uniform distribution of PC air-holes providing modulation of refractive index in slab waveguide. CQD was spin-coated with nominal thickness of  $\sim 80$  nm.

The samples of CQD-PC laser patterned by laser holographic lithography technique did not have profound quality for further measurements. SEM images of  $\text{Si}_3\text{N}_4$  PC backbone showed non-uniform PC air-holes lacking enough space for  $\text{Si}_3\text{N}_4$  high index material in slab waveguide. CQD spin-coating was not conducted for these LHL-fabricated samples; however, I will use this for CQD over-layer thickness analyses.

Measurement results, further analyses and experiments are to be discussed in the Chapter 4.

## References

1. J. Lim, S. Jun, E. Jang, H. Baik, H. Kim and J. Cho, "Preparation of highly luminescent nanocrystals and their application to light-emitting diodes", *Adv. Mater.*, **19**, 1927 (2007).
2. K. S. Cho, E. K. Lee, W. J. Joo, E. Jang, T. H. Kim, S. J. Lee, S. J. Kwon, J. Y. Han, B. K. Kim, B. L. Choi and J. M. Kim, "High-performance crosslinked colloidal quantum-dot light-emitting diodes", *Nat. Photonics*, **3**, 341 (2009).
3. S. R. J. Brueck, "Optical and interferometric lithography-Nanotechnology enablers", *Proceedings of the IEEE*, **93**, 1704 (2005).
4. T. C. Hennessy, *Lithography : Principles, Processes and Materials*, (Nova Science Publishers, Inc., 2011).
5. M. Kyungtaek, "Photonic Crystal Phosphors", 서울대학교대학원, 2015.
6. C. O. Cho, J. Jeong, J. Lee, H. Jeon, I. Kim, D. H. Jang, Y. S. Park and J. C. Woo, "Photonic crystal band edge laser array with a holographically generated square-lattice pattern", *Appl. Phys. Lett.*, **87**, 161102 (2005).

# Chapter 4

## Measurements, Results and Discussion

### 4.1 Introduction

In this chapter, fabricated CQD-PC lasers are evaluated if they show properties in accordance with the design. Two types of fabricated CQD-PC devices are examined: types of different thickness of the deposited CQD films. Spin-coating of CQDs encompasses inherent CQD over-layer issue, and as mentioned in earlier chapters, the issue must be addressed in order to fully explain properties of laser operation.

At fabrication stages, thickness of CQD over-layer is quite speculative property. Thickness of spin-coated CQD on PC backbone would yield different results from the same process performed on a planar surface. Nominal thickness  $\sim 80$  nm does not mean exactly matching 80 nm-thick CQD over-layer. However, testing the CQD thickness on a PC backbone prior to the same process of fabricating another “real” CQD-PC laser device is simply not practical.

First, it was necessary to verify that CQDs were filling air-holes of PC backbone in order to ensure lasing mode generation by proper fabrication of designed CQD-PC structure. This step is confirmed by “scratch test” shown in Fig 3-2-3 in the previous chapter. Hence, it is fair to say that nominally 80nm-thick spin-coated CQD film seemed to fill air-holes as intended, and yet the over-layer thickness is unknown.

Another important part of the CQD over-layer issue is overall physical feature

of CQDs on top of PC cluster. It is assumed that CQDs form planar film on a surface, and this is probably true for planar backbone. However, on a PC cluster, CQDs might form again a planar film, a PC transferred groove pattern, or even mixture of local grooves and planar CQD film formation depending on overall amount of CQDs used for spin-coating process.

For laser characterization, this chapter presents laser spectra with various levels of optical pumping power density along with light-in versus light-out characteristic curves. Verification of the thickness of CQD over-layer was based on the CQD thicknesses of CQDs on a planar part of fabricated device samples by SEM cross-sectional images analyses.

## 4.2 Measurements and Results

### 4.2.1 Micro-photoluminescence setup

Fabricated devices were optically pumped using a frequency-doubled (532 nm) Nd:YAG laser in a pulsed mode (pulse duration 400 ps; repetition rate 1 kHz). A 10× objective lens (NA = 0.31), oriented at 45° to the surface normal, was used to excite an individual PC pattern, while emission signal was collected from the surface normal direction. An experimental setup to measure micro-photoluminescence ( $\mu$ -PL) was prepared as depicted in Figure 4-2-1 in order to characterize fabricated CQD-PC band-edge lasers. Light emission data from the laser was collected to a spectrometer (DW700, Dongwoo Optron) for 3 sec. The focusing lens was intentionally off-focused such that pump spot size became about  $60\ \mu\text{m} \times 80\ \mu\text{m}$  on the sample surface, somewhat elongated due to the oblique incidence but still large enough to cover an individual PC pattern ( $50\ \mu\text{m} \times 50\ \mu\text{m}$ ).

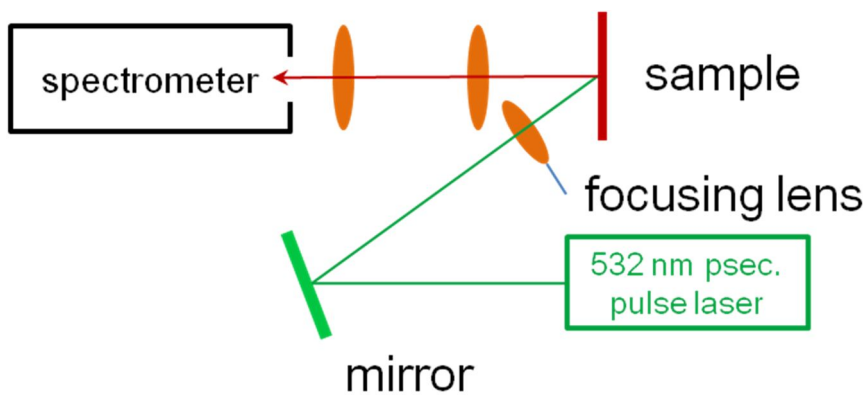


Figure 4-2-1 Micro-photoluminescence ( $\mu$ -PL) measurement setup a 532 nm, frequency-doubled, 400 pico-second pulsed Nd:YAG laser with 1 kHz repetition rate to characterize laser emission from CQD-PC band-edge lasers.

## 4.2.2 Measurement of CQD-PC laser with nominal 80 nm-thick CQD over-layer

At first, as already explained in Chapter 3, a CQD-PC device was spin-coated targeting nominal CQD thickness  $\sim 80$  nm. This was already presented in the previous chapter explaining the details of fabrication method. Figure 4-2-2 shows typical measured spectra, which shows high peaks at two distinct wavelengths. Light input vs. light output ( $L-L$ ) characteristic curve shows clear evidence of laser operation, as shown in Figure 4-2-3.

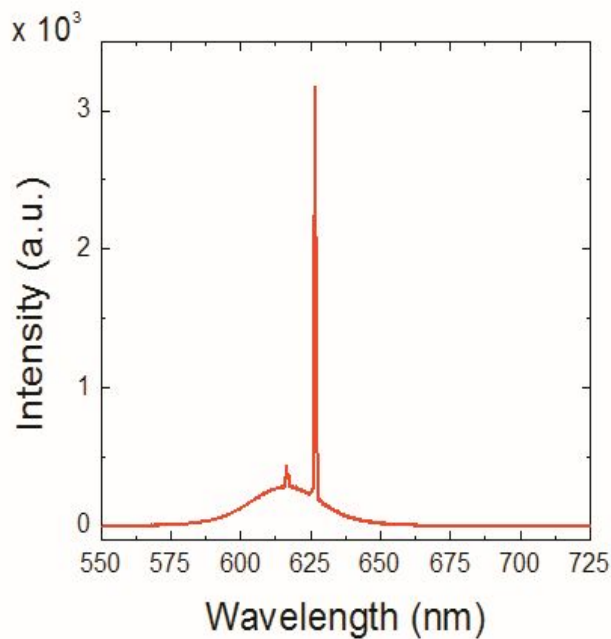


Figure 4-2-2 Micro-photoluminescence spectra measured from the CQD-PC band-edge laser devices at various pump power density levels. Nominal CQD over-layer thickness  $\sim 80$  nm

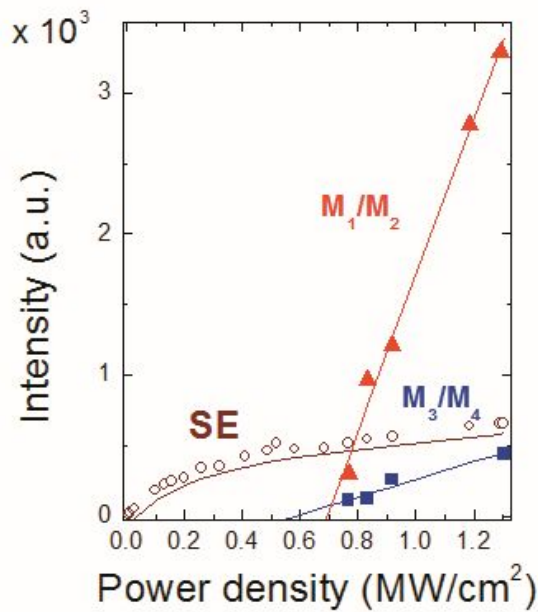


Figure 4-2-3  $L$ - $L$  curve recorded from the CQD-PC laser devices with nominal CQD over-layer thickness  $\sim 80$ nm

The spectral separation  $\Delta\lambda$  between the two lasing modes is measured to be  $\sim 11$  nm, which is close to the simulated M-point band-gap of  $\sim 12$  nm—Fig. 2-3-3c. The two major laser lines were therefore identified as the two band-edge modes on both sides of the M-point band-gap:  $M_1/M_2$  (HIBE modes) for the long wavelength laser line and  $M_3/M_4$  (LIBE modes) for the short wavelength laser line. Here,  $M_1/M_2$  modes showed dominant lasing operation with laser threshold  $\sim 0.7$  MW/cm<sup>2</sup> as shown in Fig 4-2-3. The  $M_3$  and  $M_4$  bands are degenerate modes as previously explained. Due to 4-fold symmetry of 2D square lattice, the only difference of two orthogonal modes with the same energy is different wave vectors pointing  $k_{||} = (1, 1)$

and (1, -1).

One important fact must be addressed; the strength of spontaneous emission in Figs. 4-2-2c and 2d is exaggerated relative to the laser intensities due to directionally isotropic spontaneous emission. Hence, its detection efficiency in the surface-normal direction is much better than for the lasing M-point band-edge modes whose propagation directions are along the wafer plane. For data-sorting of  $L-L$  curve in Fig 4-2-3, spontaneous emission was subtracted from the peak value at two lasing wavelengths, so as to fairly reflect light emission level of each type. Therefore, there is no ‘below threshold’ data in the  $L-L$  curve.

As lasers, CQD-PC devices show a particular polarization. Figure 4-2-4 shows that devices emit light with horizontal polarization. It seemed that laser emission with upward  $\mathbf{k}$  vector with electric field oscillating in the horizontal direction is scattered off the trench of mesh grid. Due to scattering of the laser,  $\mathbf{k}$  vector became pointing surface normal maintaining the field oscillation direction, hence collected data showed the above result: polarized laser emission in horizontal direction.

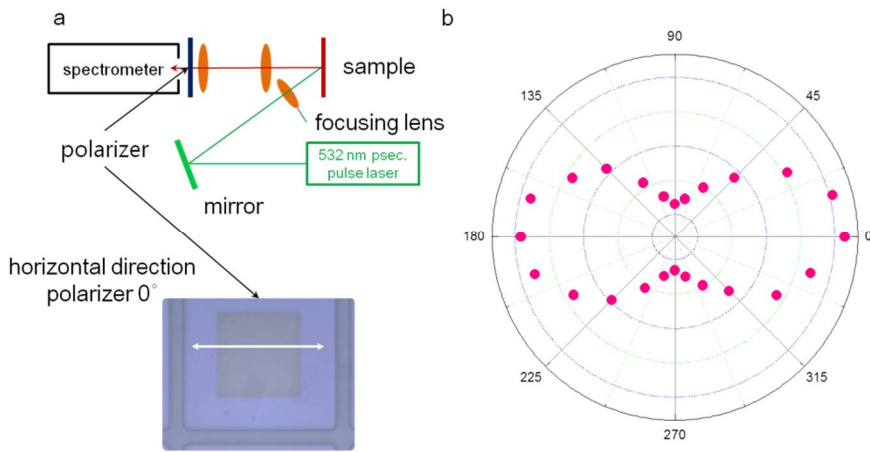


Figure 4-2-4 Polarization properties of CQD-PC band-edge lasers. (a) measurement setup with polarization analyzer in front of spectrometer (b) polar plots of lasing CQD-PC emission showing horizontal dipole polarization

#### 4.2.3 CQD over-layer analyses: T-130 device

It was already confirmed in Chapter 3 that CQDs were filling air-holes tightly without any void of PC backbone. Because it was important to ensure complete filling of air-holes in the PC backbone, nominal thickness  $\sim 80$  nm was determined to provide sufficient amount of CQDs over the entire device. Feature of such CQD film, filling air-holes of PC backbone, was confirmed by SEM and AFM analyses, however the measured thickness of CQD over-layer was proven to be different from the nominal thickness  $\sim 80$  nm.

For further discussion, I focus on a closer look on CQD over-layer. Figure 4-2-5 shows analyses revealing the real situation over a device. Figure 4-2-5c is an

already introduced back in the previous chapter. I performed atomic force microscopy (AFM) analysis to confirm the thickness of CQD over-layer on a PC cluster, and Fig 4-2-5b shows the cross-sectional information along the red line on a surface image of AFM analysis in Fig 4-2-5a. Figure 4-2-5d presents a cross-sectional image of CQD over-layer on a planar surface. These results clearly show that the thickness is  $t_{\text{CQD}} \approx 130$  nm. For convenient discussion from now on, this CQD-PC laser sample is to be called T-130.

Mode transition depending on CQD over-layer thickness still return similar feature of lasing modes. Although HIBE and LIBE modes shows red-shift according to 3D FDTD analysis with varying CQD layer on top as shown in Fig 4-2-6, two modes still remain in gain bandwidth of CQD.

I suppose a hypothesis that a thinner CQD over-layer of a device sample in the same batch of fabrication would yield rather LIBE-dominated lasing operation. The T-130 device seemed to show HIBE dominated laser operation due to its “thick” CQD over-layer. In an ‘ideal device’ with zero CQD over-layer thickness, it would be much harder for CQD-PC structure to support and sustain HIBE lasing modes because CQD gain material and nodes of electric field intensity would not be overlapped.

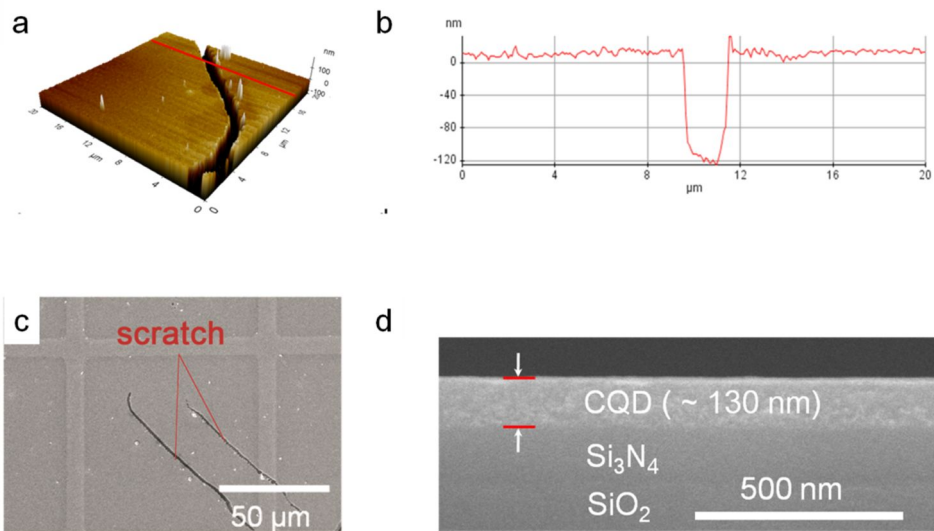


Figure 4-2-5 CQD over-layer analyses with various methods. (a) AFM image of CQD over-layer on a PC cluster (b) AFM cross-sectional depth data along the red line in (a) (c) SEM image of a device top-view of nominal CQD over-layer thickness  $\sim 80$ nm (d) SEM image of cross-sectional layers showing 130 nm CQD over-layer thickness

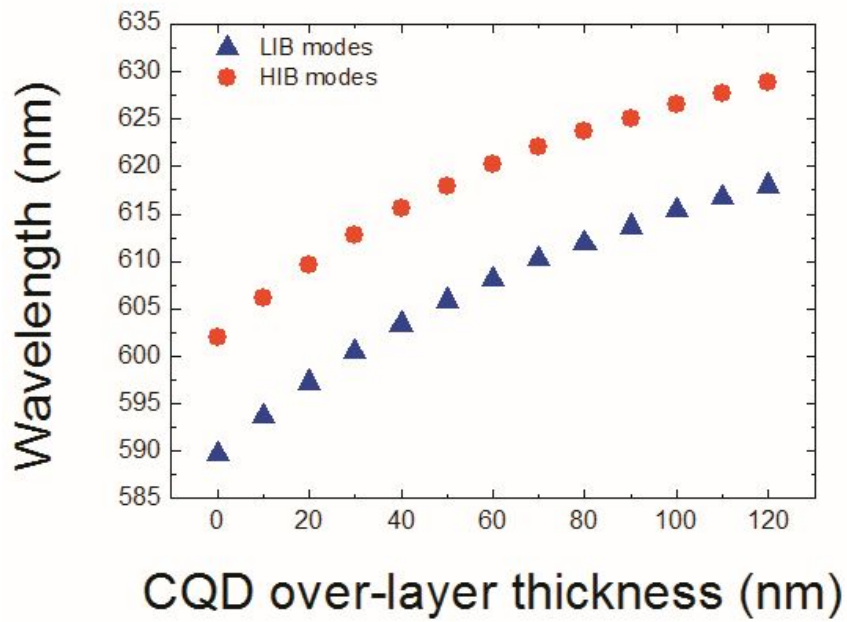


Figure 4-2-6 Mode transition of CQD-PC band-edge laser devices with various over-layer thicknesses.

#### 4.2.4 Measurement of CQD-PC laser with nominal 60 nm-thick CQD over-layer

Next, a CQD-PC device was spin-coated with CQD targeting nominal thickness  $\sim 60$  nm, which is slightly thinner spin-coating condition than the previous T-130 device. To determine whether the hypothesis suggested in the previous section, it is necessary to test CQD-PC structure with ‘thinner’ CQD over-layer thickness. No matter how thin it may be, thinner nominal thickness targeting spin-coating condition was expected to yield CQD-PC device samples with thinner CQD over-layer. Figure 4-2-7 depicts such processes, in which cyclohexane concentration was the control factor as explained in Chapter 3.

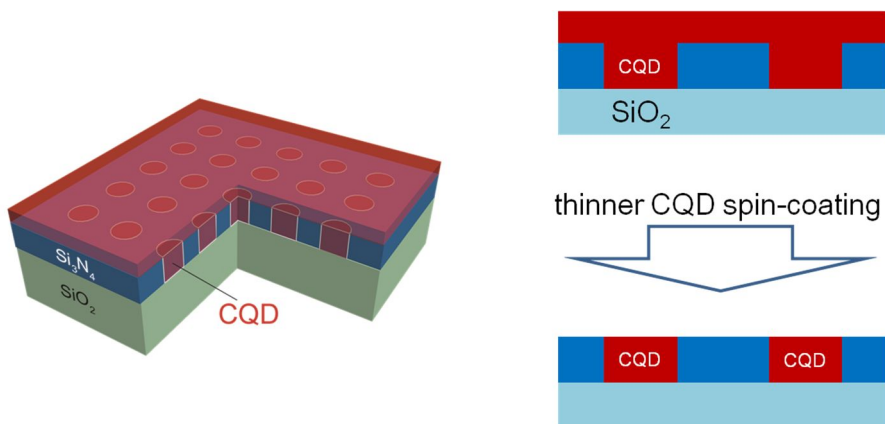


Figure 4-2-7 An ‘ideal device’ realized by CQD spin-coating process for an over-layer thickness thinner than T-130. For an ‘in-reality’ sample fabrication, nominal CQD thickness was set to be  $\sim 60$  nm.

In contrast to the T-130, this one does not really show a clear spectral separation  $\Delta\lambda$  and the two lasing modes. However, the dominant lasing operation is occurred at shorter wavelength  $\lambda \sim 618$  nm close to the simulated  $M_3/M_4$  band-edge modes in Fig. 2-3-3c. The LIBE mode was appeared first along with increase of pump power as I expected from the hypothesis for a thinner CQD over-layer. This time, an  $M_3$  or  $M_4$  mode showed dominant lasing operation with laser threshold  $\sim 2.5$  MW/cm<sup>2</sup> as shown in Fig 4-2-9. This laser threshold is approximately 4 times higher than that of T-130.

Because the same set-up was used for micro-photoluminescence, the strength of spontaneous emission spectra in Figs. 4-2-9 is also exaggerated relative to the laser intensities. However, detected level of spontaneous emission is lower than the level of T-130, quantitatively half of T-130, probably due to decreased total amount of CQDs from the spin-coating process.

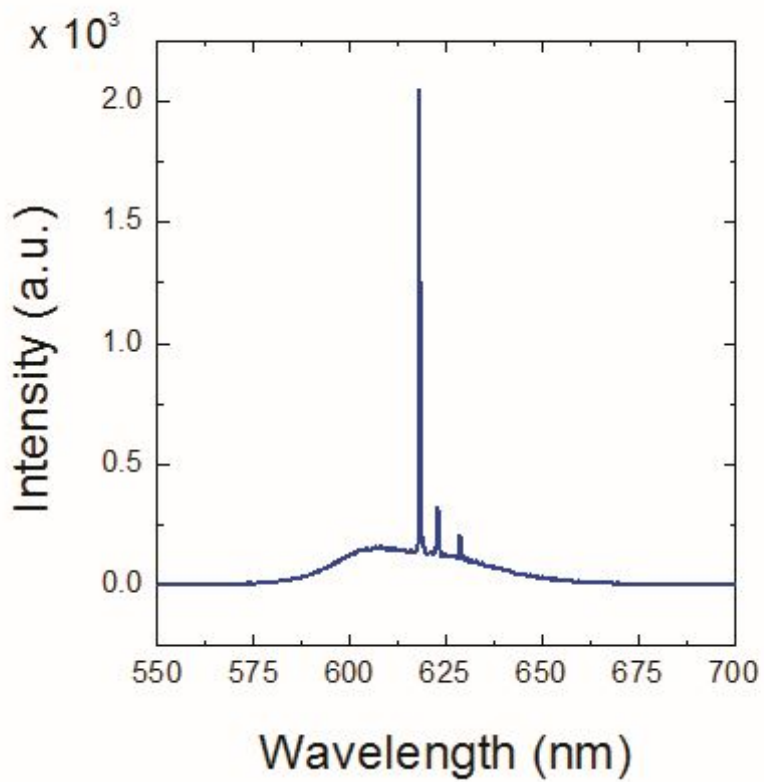


Figure 4-2-8 Typical micro-photoluminescence spectra measured from the CQD-PC devices at various pump power density levels. Nominal CQD over-layer thickness  $\sim$  60nm

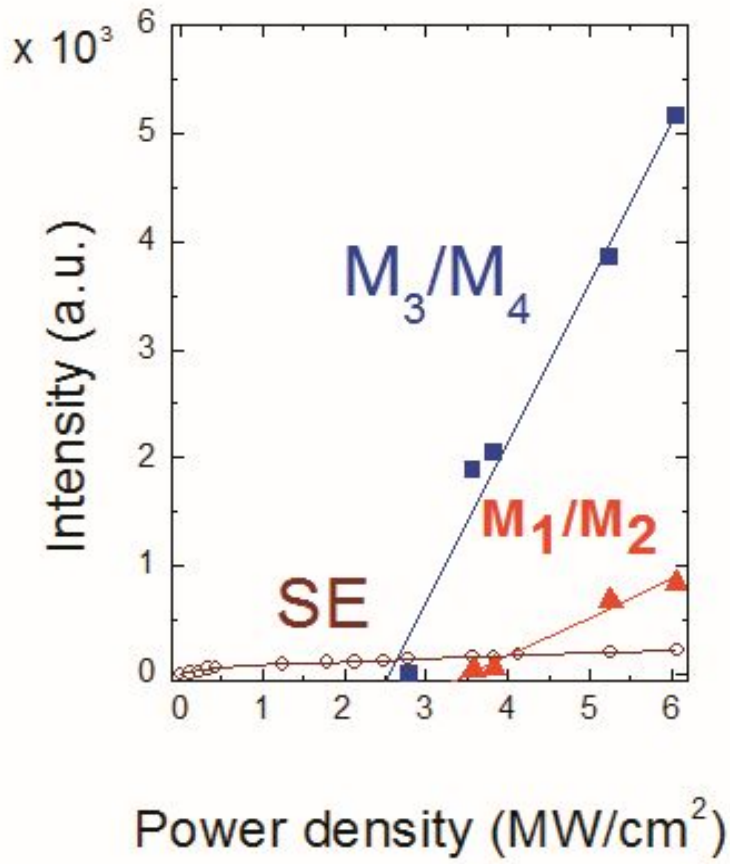


Figure 4-2-9 *L-L* curve recorded from the CQD-PC laser devices with nominal CQD over-layer thickness  $\sim 60\text{nm}$

#### 4.2.5 CQD over-layer analyses: T-80 device

This time, I focus on a closer look on CQD over-layer of the sample spin-coated by  $\sim 60$  nm nominal thickness recipe. Figure 4-2-9 shows the cross-sectional image of CQD film on planar part of device samples. It clearly shows that the thickness is  $t_{\text{CQD}} \approx 80$  nm, again slightly thicker than nominal  $\sim 60$  nm, but at the same time definitely thinner than T-130. For convenient discussion from now on, this CQD-PC laser sample is to be called T-80.

Due to the limited number of samples available direct SEM analysis on a T-80 sample was not possible. Although Fig 4-2-10 shows the CQD over-layer but not the layer directly on top of PC cluster. In order to confirm CQDs filling and discuss CQD over-layer feature on PC cluster, the samples fabricated by LHL method were also spin-coated with CQDs using the same spin-coating condition for the same nominal CQD over-layer thickness. Figure 4-2-11 shows the top and cross-sectional views of layers.

Figure 4-2-11 indicates that CQD over-layer on T-80 can be groovy, at least partially on PC cluster but planar on non-PC region. As shown in Fig 4-2-11a, the feature of top surface shows that non-uniform pattern of PC clusters was directly transferred to CQD over-layer with some of disconnected CQDs because of too large air-holes, and even air-hole boundaries touching each other. Despite imperfect nature of top CQD over-layer, CQDs were completely filling air-holes of PC backbone. Figure 4-2-11b and 11c assures perfect CQD filling with groovy character of CQD over-layer, which is completely different from CQD over-layer of T-130; In T-130 case, CQD over-layer was thick enough to show no groovy patterns

of CQDs in over-layer were visible.

This leaves a room for further optimization of CQD spin-coating condition for fabrication. Considering the initial testing of CQD spin-coating introduced in Chapter 3 left partial void (nominal thickness then was  $\sim 30$  nm.), the optimal solvent concentration could be found somewhere in between 40  $\sim$  60 nm nominal thicknesses. Of course, this concentration for nominal thickness could be an issue for each run of fabrication process because control by solvent concentration is dependent on status of CQD synthesis and types of solvent. Detailed optimization is out of the scope of this study to show proof-of-concept device design and laser operation.

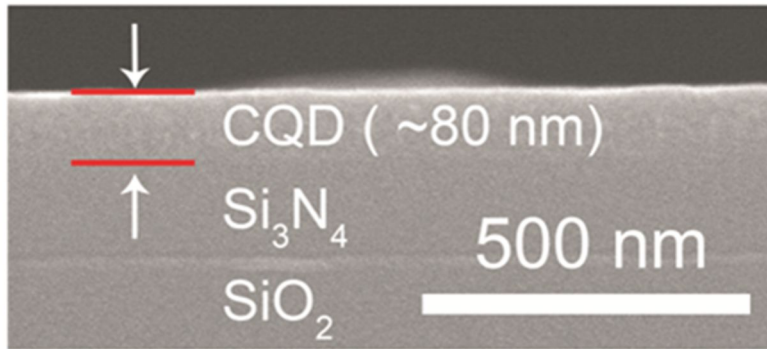


Figure 4-2-10 SEM image of cross-sectional layers showing 80 nm CQD over-layer thickness: T-80

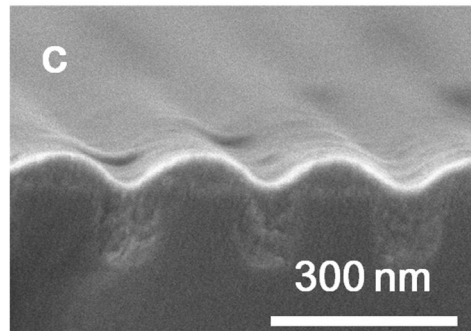
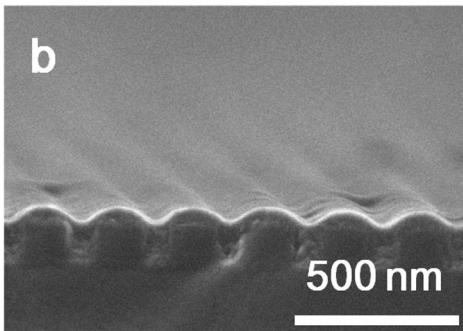
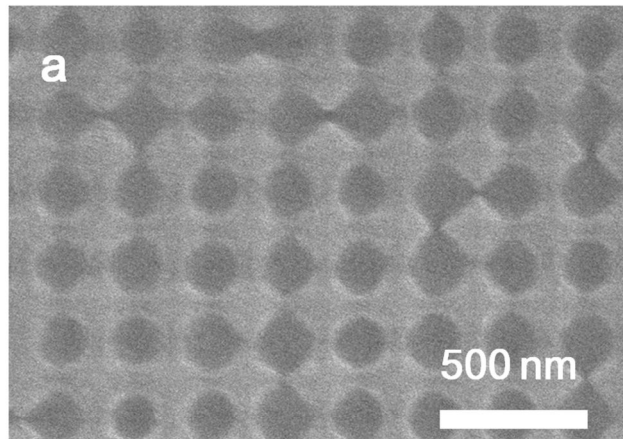


Figure 4-2-11 SEM images of CQD spin-coated devices fabricated by LHL method. (a) a top-view SEM image on 2D PC backbone (b)(c) SEM images of cross-sectional layers showing  $\sim 60$  nm CQD over-layer when spin-coated with recipes targeting nominal thickness  $\sim 60$  nm just as T-80

### 4.3 Discussion: T-80 vs. T-130

I examined two types of devices with different CQD over-layer thicknesses, which were prepared conveniently by controlling CQD concentration in cyclohexane solution (See Appendix A). Figures 4-3-1 shows the comparison of T-180 and T-130 with cross-sectional SEM images and micro-photoluminescence spectra under various optical pumping power densities. Above thresholds as shown in Fig 4-3-1c and Fig 4-3-1d, two distinct, sharp laser lines appeared for the both of T-80 and T-130 devices.

The dominant lasing mode is switched between T-80 and T-130 in Figs. 4-3-1c and 1d, which proves the hypothesis on relationship between mode identification and CQD over-layer thickness. In a situation that the CQD over-layer thickness is zero, that means CQDs fill air-holes only, it is highly unlikely for  $M_1$  or  $M_2$ , HIBE modes to lase because overlapping of  $|E_1|^2$  with optical gain is negligibly small. It leaves either the  $M_3$  or the  $M_4$  band-edge mode (LIBE modes) for the only possible lasing mode in PC slab. Picking up either one of LIBE modes depend on a specific, real-time situation of a lasing experiment.

If a few tens of nanometer-thick CQD over-layer is assumed to be added, however, it is easy for HIBE modes come into play because HIBE modes in CQD over-layer are equipped with more CQDs than LIBE modes in a slab. In addition, optical pumping light first encountered CQD over-layer and then the slab underneath it due to top pumping from an angled incidence with respect to surface

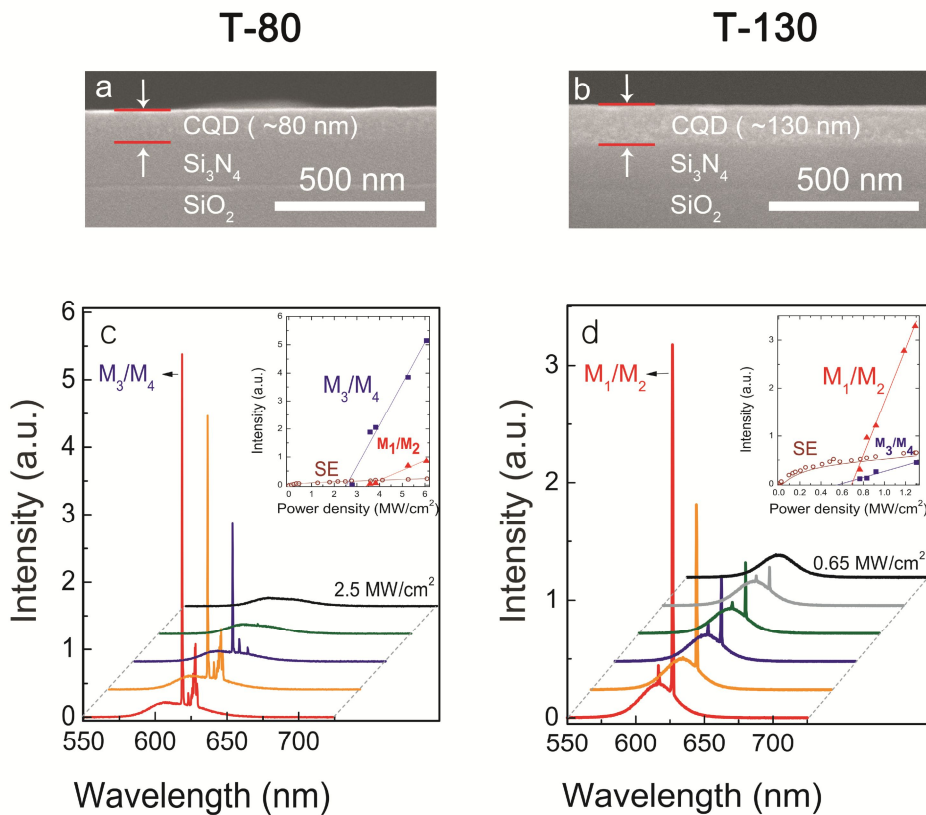


Figure 4-3-1 Lasing properties of CQD-PC band-edge lasers. (a)(b) Cross-sectional SEM images of two CQD-PC devices with different CQD layer thicknesses: (a) T-80 and (b) T-130, from which the CQD over-layer thicknesses were measured to be  $\sim 80$  nm and  $\sim 130$  nm, respectively. The SEM images were taken from planar part of samples for thickness characterization. (c)(d) Photoluminescence spectra measured from the CQD-PC band-edge laser devices at various pump power density levels: (c) T-80 and (d) T-130. The insets are light-in versus light-out ( $L-L$ ) curves drawn from the measured spectra:  $L-L$  curves for the HIBE (red, solid triangles) and LIBE (blue, solid squares) modes as well as spontaneous emission (brown, open circles).

normal direction. Both HIBE and LIBE modes can lase depending on thickness of CQD over-layer. LIBE modes are expected to be dominant with thin CQD over-layer thickness if the CQD film is uniform and clear with no void or defects. For T-80, a relatively small amount of optical gain (available due to a relatively thin CQD over-layer) makes the LIBE mode laser threshold high, which is consistent with the high threshold value given in Fig 4-2-8 and the inset of Fig 4-3-1d. In Fig. 4-3-1c that some complex laser modes appear in addition to the two major lasing modes, which could be subjected to the Fabry-Perot oscillation modes developed across the entire PC pattern as a result of high levels of optical excitation, but at the same time relatively insufficient amount of optical gain available to HIBE modes.

As CQD over-layer becomes fairly thick, comparable to or thicker than the air-hole depth, as the case for T-130 in Fig. 4-3-1b, however, optical gain available should become higher and at the same time spatially more homogeneous so that the both groups of band-edge modes can lase at relatively low thresholds as in Fig. 4-3-1d. On the other hand, the HIBE modes ( $M_1$  or  $M_2$ ), whose Q-factors are slightly higher, are likely to lase first, take most of the available gain, and thus become dominant; Q-factors estimated from FDTD computer simulations on the corresponding “cold” PC structure—the imaginary part of CQDs are not contributing to overall circumstances of CQD-PC structure under optical pumping due to already inverted population of carriers—are  $\sim 1,800$  and  $\sim 1,600$  for the HIBE and LIBE modes, respectively as shown in Fig 4-3-2. Figure 4-3-1d confirms that

laser emission intensity of a HIBE band-edge mode is indeed much stronger than that of the LIBE mode. The inset of Fig. 4d indicates that laser thresholds are significantly reduced (by a factor of  $\sim 4$  when compared with those of T-80), consistent with a prediction based on FDTD numerical analyses. Detailed analyses for optical confinement factor of each mode is presented in Appendix B.

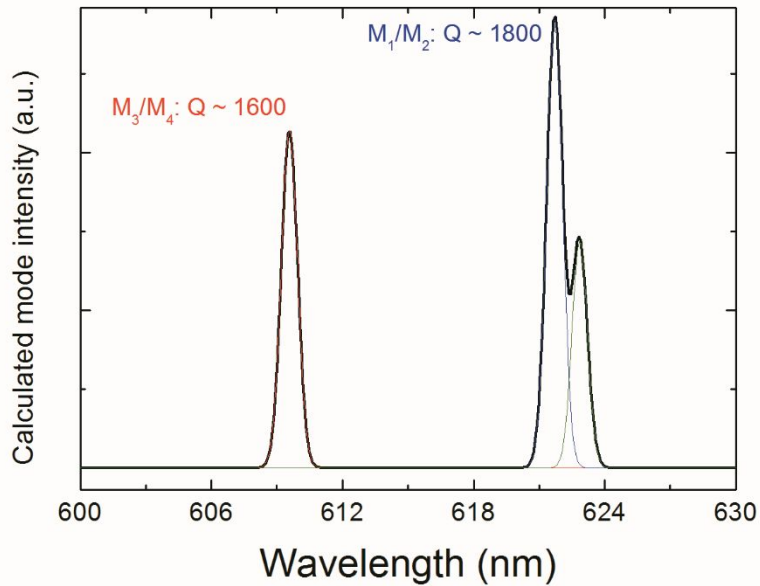


Figure 4-3-2 Quality factors for M-point band-edge modes of a “cold” cavity

# Chapter 5

## Conclusion

In conclusion, I successfully demonstrated the room-temperature lasing operation of a novel CQD-PC band-edge laser. Core-shell-shell type CdSe/CdS/ZnS CQDs were simply spin-coated as gain material on a passive 2D square lattice PC backbone slab composed of  $\text{Si}_3\text{N}_4$ . Fabricated CQD-PC devices lased at both of the HIBE and LIBE modes at M-point, as designed. The modal dominance among them was found to be dependent on the thickness of CQD over-layer, offering a convenient way how to control the lasing mode. We expect that further optimizations in structural design and device fabrication will improve laser performance and mode controllability. Unlike conventional PC lasers built on an epitaxial MQW structure, our CQD-PC lasers can be made cheap. In addition, optical gain (or CQDs) is applied extrinsically onto a pre-made passive PC backbone, which implies that spatial locations and sizes of lasers can be tailored, making the proposed device and fabrication schemes suitable and attractive for the future high density photonic integrated circuits where many active and passive photonic components are to be integrated on a single chip platform.

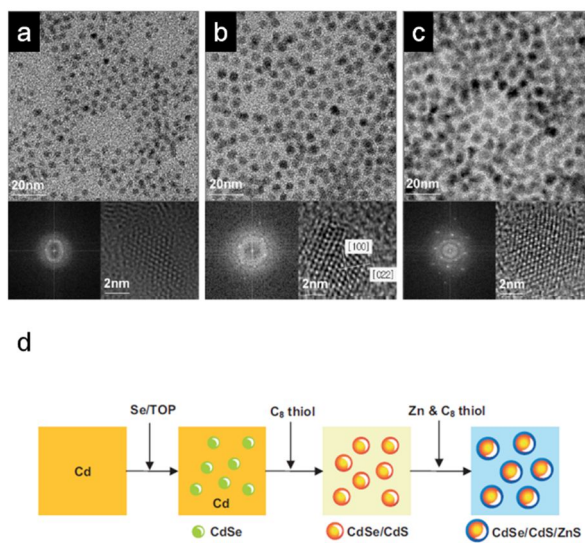
# Appendices

## A. Preparation of CQD film

I clarify that CQDs for this study was exclusively supplied by co-working researchers in Samsung Advanced Institute of Technology (SAIT).

- Synthesis (at Samsung Advanced Institute of Technology)

When it comes to CQD synthesis and film deposition, procedure in references [41, 42] of Chapter 1 are exactly followed; Details of synthesis procedure such as types, amounts, concentration, and manufacturing company information of chemical compounds, precursors, and solvents are all in complete accordance with the above references. Suppl. Figure 1 shows the overall process of CQD synthesis. CdSe/CdS/ZnS core-shell-shell CQDs are chemically synthesized. For synthesis procedure of CdSe/CdS/ZnS nanocrystal, precursor materials were consecutively employed to form core and the two shell. Detailed conditions for intricate synthesis processes are introduced in related literature written by researchers at SAIT. It is worth mention that cyclohexane was the solution used at the final stage, as the solvent of dispersing the precipitates.



**Suppl. Figure 1** Consecutive synthesis of core-shell-shell CQDs.

- Photoluminescence quantum yield

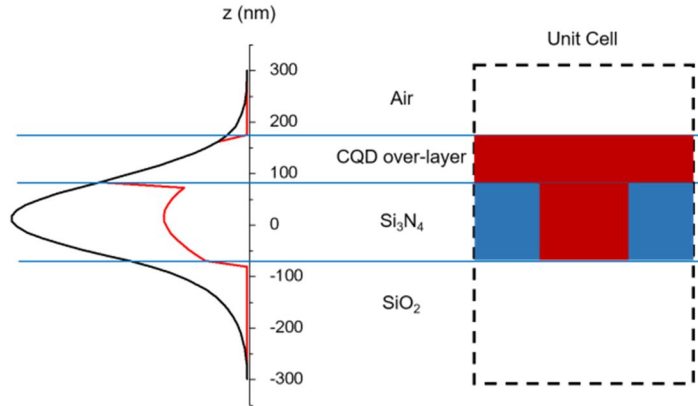
Photoluminescence (PL) quantum yield (QY) can be obtained by measuring the absorption and photoluminescence spectra of the CQDs, and subsequently comparing them with those of Rhodamine 640 dye, which is known to have a near 100% PL quantum yield. Detailed PL QY measurement sequence is described in (J. Am. Chem. Soc. 124(9), 2049-2055, 2002). From the ratios between the two materials, CQDs and Rhodamine 640, in absorption strength and integrated PL intensity, we have estimated the PL QY of our CQDs to be  $\sim 75 \pm 5\%$ .

## B. Modal gain and confinement factor

Pure material gain  $g$  of CQDs depends on the level of optical excitation—optical power of pump beam. When it comes to a specific photonic structure such as laser cavity, however, one has to consider the optical overlap of a resonant mode with gain material as well, leading to the term “modal gain” defined by  $\Gamma g$ , where the confinement factor  $\Gamma$  for a given mode is expressed as

$$\Gamma = \frac{\text{Light intensity in the active layer}}{\text{Total light intensity}} \sim \frac{\int_{\text{active}} |E|^2}{\int_V |E|^2}.$$

I calculated values of confinement factor for M-point band-edge modes supported by T-130 and T-80 samples. In our case, gain material in a unit cell has two parts, CQD-filled cylinder and CQD over-layer as depicted in Suppl. Fig. 2; this is the volume over which the integration in the numerator is to be done. Also shown in the figure are the guided mode intensity profile (generated by FDTD calculation) and the effective mode intensity profile (after taking into account the modal overlap with gain material). Calculated optical confinement factors for T-180 and T-130 are listed in Suppl. Table 1.



**Suppl. Figure 2** An example of optical confinement calculation for the LIBE mode of T-80 sample. Black line indicates the total intensity profile of the mode, and red line is the effective mode intensity for which the areal ratio of gain material (CQD) at a given z-coordinate is taken into account.

	T-80	T-130
LIBE mode	0.392	0.428
HIBE mode	0.281	0.325

**Suppl. Table 1.** Optical confinement factors calculated by FDTD method

Assuming that optical gain  $g$  is uniform across CQD films, modal gain is directly proportional to the confinement factor itself. Then the modal gains of T-130 are higher than T-80 for both the HIBE and LIBE modes, which is consistent with the lower laser thresholds for T-130. In addition, the fact that LIBE modes have

higher modal gain values than HIBE modes explains why the thresholds of LIBE modes are lower than those of HIBE modes, regardless of the CQD over-layer thickness.

## 국문 초록

반도체 기반의 레이저 광원은 흔히 다중양자우물 구조에 의존하여 제작되고 따라서 반도체 자체의 성장 조건인 기판에 크게 의존할 수밖에 없고, 다중양자우물의 파장에 고정된 광원이 제작되는 것이 일반적인 현실이다. 본 연구는 보다 쉽고 폭넓은 나노 레이저 광원의 이용을 위하여 기판 의존성이 낮고, 원하는 파장에서의 레이저를 제작하기 위하여 콜로이드 양자점과 광자결정의 결합을 통해 이 문제를 해결하고자 하였다.

콜로이드 양자점은 반도체 나노크리스탈로서 입자의 크기에 따른 ‘양자가둠효과’에 의한 밴드갭 발광 파장 가변성이 큰 장점이다. 또한 콜로이드 양자점은 스핀 코팅 방법을 이용하여 쉽게 박막으로 제작될 수 있어 이러한 콜로이드 양자점을 이득 물질로 다중양자우물을 대체하는 구조를 만드는 데 용이하게 사용할 수 있다.

한편 광자결정은 굴절률이 서로 다른 두 가지 이상의 물질이 공간 상에서 주기적으로 배열되어 있는 광학 구조로, 광자결정의 주기성에 의해 광밴드구조에서 광밴드갭 주파수 영역이 나타난다. 광밴드갭 대역에 해당하는 빛은 광자결정 내부를 진행할 수 없으며, 이 광밴드갭 효과에 기반하여 광공진기나 도파로와 같은 다양한 종류의 유용한 광소자가 개발되어왔다. 본 연구에서는 광자 결정이 갖는 띠가장자리 모드를 이용하여 빛의 매질 내 진행 속도가 매우 느린 구조를 만들어 콜로이드 양자점의 이득 대역에 맞추어 레이저 발진이 쉽게 일어날 수 있는 구조를 만드는 데 광자결정의 개념을 사용하였다.

특히 본 학위 논문에서는, 레이저 발진을 발현시키기 위한 방법으로 정방형의 단위 구조를 가지는 이차원 광자결정을 이득 물질이 없는 유전체로 실리콘 기판 위에 제작하고 콜로이드 양자점 이득 물질을 도포한 박막을

제작하여 다중양자우물을 사용하는 여러가지 광자결정 레이저에 비해 제작 공정 상 물질의 낭비가 없는 새로운 개념의 레이저 소자를 제시한다. 다중양자우물을 사용하는 경우 이득물질인 양자우물의 일부분을 식각해야 하는 기존의 다른 방법과는 달리 높은 파장가변성과 제작 공정의 용이성이라는 두 가지 목적을 모두 달성 하는 것이 연구의 특징이다.

콜로이드 양자점을 스핀 코팅 방법으로 도포했을 때 이용할 수 있는 낮은 굴절률 밴드의 레이저 발진을 목표로 하여, 서로 다른 스핀 코팅 조건에서 양자점 박막이 이루는 두께에 따라 낮은 굴절률 모드와 높은 굴절률 모드가 각각 레이저로 발진하는 결과를 얻었다. 콜로이드 양자점이 만들게 되는 상기 잔여 박막의 두께가 얇아질수록 원래의 의도에 맞도록 낮은 굴절률 밴드에서 레이저가 되는 것을 확인하였다.

특히 본 연구는 M-point 대칭점 모드의 슬랩 내부로 진행되는 레이저로서 on-chip 소자에 응용이 용이하다. 또한 콜로이드 양자점에 바이오 물질을 부착하는 것이 가능하므로 센서로서 응용이 가능하여 향후 다양한 방식으로 본 연구가 발전할 수 있다.

**핵심어:** 광자결정, 콜로이드 양자점, 광자결정 레이저, 광밴드에지,

**학번:** 2008-20451